電析法を用いた多成分系膜の創製および酸素発生用電極への適用に関する研究

2023 年

広島工業大学大学院工学系研究科知的機能科学専攻

肖　天

Fabrication of Multi-Component Film by Electrodeposition and the Application as Oxygen Evolution Electrode

2023

Graduate School of Science and Technology,
Hiroshima Institute of Technology

Tian Xiao

Contents

Abstract

化石燃料の使用に伴って大量な二酸化炭素(CO_2)が大気に排出されている。一方、水の電気分解で得られたグリーン水素は、CO_2 排出ゼロを達成する効果的な方法である。水の電気分解は、水素発生反応(HER)と酸素発生反応(OER)が含まれる。HER に比べて、OER は不活性であり、O_2 の発生には高い過電圧が必要である。すなわち、効率よく水素を得るため、アノード電極(陽極)の触媒活性に依存する。アノード触媒としては、ルテニウム(Ru)系触媒が多用されているが、ストレージリソースの不足より、大規模な応用は制限される。したがって、高い活性、効率や安定性を備えた安価な触媒の開発が急務となっている。

近年、ほぼ等モル比の多種類元素からなるハイエントロピー合金の酸化物(HEO)、窒化物および硫化物は、酸素発生電極としての触媒活性とその安定性が注目され、多くの研究がなされている。しかし、それらを合成した際、多くは高温または高圧の処理が必要である。また、ナノ粒子は高温条件下で凝集しやすく、形態の制御が困難である。材料合成の後も電極として使用できるように導電性基板表面に接着剤を使用して固着する必要があり、電極としての導電性が低下する。上記の方法と比較して、電析法による HEO 材料の調製は、高温高圧を必要とせず、必要な設備が少なく、操作が簡単であり、電極の形状や寸法に制限がない。また、直接に導電性基板に触媒が取り付けられ、接着剤の使用に必要がない。本研究の目的は、安価の Cr、Mn、Fe、Co、Ni の遷移元素を選べ、自由に電位を印加できる有機溶媒中でワンステップ電析法を開発し、OER 用電極触媒を作成する。また、得られた電極に対して機械特性および酸素発生触媒活性を評価し、OER 触媒としての稼働機構を考察する。

本研究では、支持電解質 LiClO4 の有無という 2 種の浴液(溶媒：DMF (N, N-ジメチルホルムアミド)と CH_3CN (アセトニトリル))中、所定電位下で酸素含有型 CrMnFeCoNi 膜を銅板上に電析した。得られた 2 種類膜の表面形態、成分や結晶構造を SEM、XRD、EDS、TOF-SIMS および TEM で調べた。浴液中に $LiClO_4$ がない場合では、膜にナノ結晶をもつアモルファス構造が確認された。一方、$LiClO_4$ のある浴液中で得られた膜は、内層、中間層、外層に分け、内層では酸化リチウム、

外層では酸化リチウムや炭酸リチウム、O、Cr、Mn、Fe、Co、Ni の均一な空間分布は主に中間層に含まれた。また、この膜は水中では銅から剥離しやすく、電子照射に対して不安定である。続いて、上記の浴液中で酸素を含む CrMnFeCoNi 膜の電析合成に及ぼす電析電位およびリチウムイオンの影響を調べた。その結果、浴液に $LiClO_4$ がある場合、膜はいずれの合成電位においても水中で不安定であった。これによって、$LiClO_4$ が本研究の電析プロセスにおいて、支持電解質として不適切であることがわかった。一方、$LiClO_4$ を使用しない場合、浴液中の金属イオン濃度を高めることによって、水中でも安定な酸素含有型 CrMnFeCoNi 膜が各電位化下で得られた。いずれの膜表面から均等的な球状粒子が観察された。また、電析電位の卑化とともに粒子がやや大きくなり、厚さも増えた。膜中での金属元素の含有率は、Cr、Mn、Fe、Co およびNi はそれぞれ約 3%、2%、6%、4%および 11%であり、酸素と炭素はそれぞれ約 55%と 16%である。また、XPS 分析によると、すべての Cr、Mn と Fe は酸化状態にあり、Co に酸化状態と金属状態が共存し、また Ni はほぼ金属状態である。一方、最大荷重 40 nN で得られた膜のプラスチック硬度は、銅基板の硬度 1600MPa より、2670 MPa (-2.0 V vs. SSE)、2660 MPa (-2.5 V)、および 2250 MPa (-3.0 V) である。この酸素含有型 CrMnFeCoNi 膜を水分解の OER 電極とし、アルカリ性 KOH 水溶液中でリニアスイープボルタンメトリー(LSV)曲線を測定し、常用の酸化ルテニウム(RuO_2)電極よりも高触媒活性が確認された。

上記を要約すると、本研究は酸素含有型 CrMnFeCoNi 膜ワンステップ法で合成できた。また、OER 電極として、この膜を高い触媒活性が確認された。

本論文は、序文(第 1 章)と結論(第 4 章)を含み、4 章で構成されている。第 2 章では、有機溶媒中の支持電解質 $LiCLO_4$ は、所定の電析電位で安定な膜の作成に不利であることを明らかにした。これを踏まえて、$LiCLO_4$ を使用しない浴液を構築し、酸素含有型 CrMnFeCoNi 膜を銅基板に合成した。また、得られた膜の成分および結晶構造を調べた。第 3 章では、有機溶媒の支持電解質の有無や種々の電析電位は、皮膜の成分、結晶構造及び化学結合状態に及ぼす影響を明らかにした。また、$LiCLO_4$ を使用しない浴液を使って銅基板に合成した酸素含有型 CrMnFeCoNi 膜の作成条件を確定した。この膜は、酸素発生電極そして優れた低い過電位を有することを確認した。このように、支持電解質を使用せず、酸素を含むアモルファス

型 CrMnFeCoNi 膜の作製方法をワンステップで確立した。また、酸素を含む CrMnFeCoNi 膜を水の電気分解の酸素発生(OER)電極として適用し、高い触媒活性を確認した。

Chapter 1 Introduction

1.1 General Background of Energy Development

Renewable energies, such as green hydrogen, solar, wind, and geothermal, are obtained from nature and are inexhaustible, with higher replenishment efficiency than consumption rate. [1)] Before the Industrial Revolution (18th century), people relied on the workforce, animals, water, and wind power. After Watt improved the steam engine in 1769, coal and other fossil fuels were used to drive machines, showing a new level of human civilization. However, with the improved wealth and comfortable life, human beings began to face environmental problems like water pollution, air pollution, and global warming. [2)]

Even then, people had recognized that the reserves of fossil fuels on the earth are limited. [3)] However, the importance of finding alternative energy sources for sustainable development was still low, considering that the fossil fuel resources at that time were still sufficient, and the unknown reserves could be found with the developing exploration technology. Since the two oil crises occurred in the 1970s, people have noticed the importance of renewable energy again. However, the highly elevated oil prices reduced the demand for petroleum fuels. As a result, renewable energy finally lost its economic incentive. [4)]

In recent years, excessive fossil fuels have caused vast carbon dioxide (CO_2) emissions. The so-called global warming is bringing about extreme climate change in various places. The ecological world is substantially threatened. This situation pushes people to consider conserving energy and reducing CO_2 emissions. At this point, renewable energy development is once again highly valued. [5-8)]

As early as 1974, the Japanese government launched an engineering energy strategy. This policy aimed to develop utilization technologies of inexhaustible clean energy, including photovoltaic power, wind power, geothermal power, and hydrogen energy generation. [9)] One hundred ninety-seven countries signed a new climate agreement,

"Glasgow Climate Convention" in 2021, in which the most significant single factor affecting climate change is the increasing use of coal, therefore asking countries to reduce global greenhouse gas emissions rapidly, deeply, and continuously, and aiming to reach net zero emissions at around 2050. [10-14)] Moreover, with the Ukrainian-Russian War occurring in 2022, the energy crisis comes again; more funds are being invested in renewable energy. [15-16)]

It is worth mentioning that renewable energy is not equal to so-called green energy. The latter refers to clean energy only that does not damage the environment. Therefore, biomass energy, dam hydropower stations, and nuclear power plants cannot be strictly called green energy. On the other hand, hydrogen combustion only produces water, which does not cause environmental pollution. However, due to the high activity of hydrogen gas, most hydrogen exists in water, methane, and fuels. Only hydrogen from wind and solar energy can be called green hydrogen. [17-20)]

Even though the hydrogen element was discovered in the 16th century, the term "hydrogen" did not exist then. Henry Cavendish obtained in 1766 a "flammable gas" from the reaction between metals and acids. In 1783, Antoine-Laurent de Lavoisier confirmed Cavendish's experiment and named this element "Hydrogen". [21)] During the oil crisis in the 1970s, John Bochris first proposed the "hydrogen economy" and described the idea of hydrogen energy replacing fossil fuels. Hydrogen energy is developed through both the process and the application of research, which can be applied in chemistry, physics, engineering, industrial applications, and medical care. Nowadays, the research and development of fuel cells are hot. [22)]

Hydrogen gas can be obtained by reforming hydrocarbon fuels or by non-recombination methods such as biomass gasification, thermal cracking, hydrolysis, and water electrolysis. [23-24)] Although hydrogen gas is colorless, it is often named by the color of its source, as grey, brown, blue, green, and red hydrogens. [25)]

The grey hydrogen, the most produced hydrogen globally, is produced from natural gas through steam. Ten tons of CO_2 are released for every ton of hydrogen produced. Brown hydrogen is produced from fossil feedstocks and is one of the "dirtiest" forms of hydrogen. Brown is the color of lignite, from which CO and CO_2 are emitted. Blue

hydrogen is refined based on grey hydrogen. The carbon dioxide produced during its production does not enter the atmosphere directly but is stored. However, current carbon capture and storage processes are controversial because of the risk of safely storing CO_2 underground for hundreds of years. Another problem is the production of grey and blue hydrogen emits methane, which has an 86 times greenhouse effect greater than CO_2. In this meaning, blue hydrogen is 20% more harmful to the atmosphere than brown hydrogen. From the climate protection perspective, green hydrogen is the star among hydrogen. It is produced through water electrolysis, and the energy required can come entirely from renewable solar sources. Therefore, to a large extent, it is considered one of the key energy sources to combat global warming, and it is an effective way to achieve zero carbon emissions. Red hydrogen, like green hydrogen, is also produced through electrolysis. However, the energy it requires comes from nuclear power plants. [22-26)]

As a clean energy, green hydrogen energy has an irreplaceable and vital position now and in the future. This chapter reviews hydrogen energy, water electrolysis, and high-entropy alloys and their oxides.

1.2 Review of Hydrogen Energy and Water Electrolysis

As described in Section 1.1, due to the technological development of renewable energy, such as solar energy, various facilities are now being constructed in Japan, and solar power generation modules have been installed at homes. Moreover, the surplus electricity generated by solar energy can be used directly to produce hydrogen in electrolyzes, prohibiting carbon emissions and avoiding waste. In addition to using renewable energy for power generation, short-term storage in secondary batteries (from day to night) and power generation to electrolyze water to produce hydrogen are used. [27-28)]

Hydrogen shows high energy density per unit volume, and large-scale storage has low self-consumption. Therefore, energy can be stored in the form of hydrogen for an

extended period, and by operating a fuel cell using the generated hydrogen, electricity can be generated regardless of location and climate.

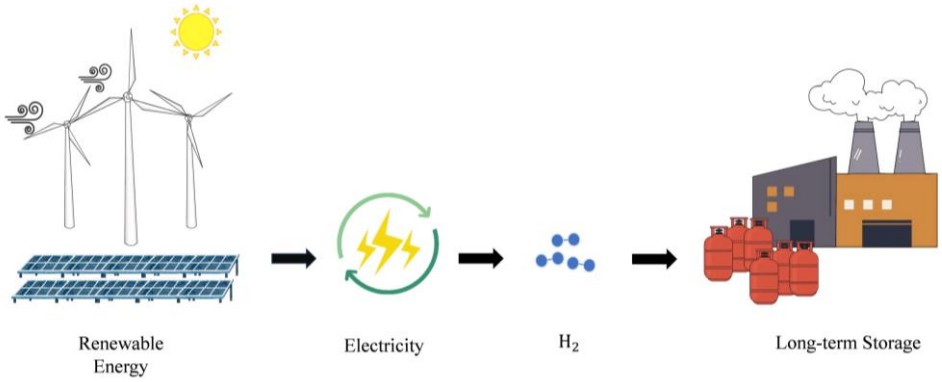

Fig 1.1 Electricity usage flowchart generated from renewable energy.

In 2017, Japan formulated the first hydrogen energy national strategy, the Hydrogen Energy Basic Strategy. [29)] In the following years, China hosted the Hydrogen Energy Ministerial (HEM) and played a leading role in building a global hydrogen society, including creating momentum for top-down hydrogen policy. [30)] During this past period, the 2050 carbon neutrality declaration was released in October 2020. [31)]

In February 2022, Russia invaded Ukraine, and changes occurred in the world's energy supply and demand structure to gradually eliminate energy dependence on Russia. Europe and the UK have significantly raised hydrogen production targets, while the US has accelerated hydrogen production with unprecedented tax incentives following the Inflation Reduction Act. The European Commission will also adopt a Green Deal industry plan. [32)]

The "Long-term Energy Supply and Demand Outlook", published in 2015, pointed out that by 2030, Japan's energy self-sufficiency rate will increase to 22-24%. At the COP21 (The 21st Conference of the Parties to the United Nations Framework Convention on Climate Change), it was agreed that by 2030, Japan's carbon dioxide and other greenhouse gas emissions will be reduced by 26% compared with the level in fiscal 2013. [33-34)] In addition, in 2016, the Hydrogen Energy and Fuel Cell Strategic Roadmap aimed to introduce fuel cell vehicles, hydrogen refueling stations, and

stationary fuel cells. [36-36)] In order to introduce renewable energy to build a large-scale hydrogen society and reduce CO_2 emissions, research on hydrogen production and storage systems that efficiently utilize renewable energy is ongoing, as described in Section 1.1. Among them, hydrogen production by water electrolysis, as a part of electric gas production, plays an essential role in direct utilization.

The electricity-to-gas demonstration experiment has also recently been mainly promoted in Germany. [37)] Power-to-gas is a technology for using or storing energy for various purposes by producing and storing hydrogen from renewable sources in hydrogen or methanation. From the second half of the 1980s to the 1990s, Europe carried out hydrogen production demonstration tests for large-scale deployment of renewable energy storage and transportation. [38)] Since 2010, electricity-to-gas demonstration experiments have been mainly carried out in Germany, aiming to effectively utilize the surplus power of variable renewable energy, mainly solar and wind, to build a low-carbon energy system. Power-to-gas can be thought of as CO_2-free production of hydrogen from renewable electricity.

1.2.1 Principle/Characteristics of Water Electrolysis

The water electrolysis systems are classified into three types: Proton exchange membrane (PEM) electrolyzers, alkaline water electrolyzers (AWE), and solid oxide electrolyzer cells (SOEC). [39-43)] This study, devoted to developing electrode catalyst materials for alkaline electrolysis batteries, will describe alkaline water electrolysis batteries in detail. In water electrolysis for AWE, two semi-electrochemical reactions, hydrogen evolution reaction (HER) and oxygen evolution reaction (OER), [44)] are included in water splitting as follows:

$$\text{Anode: } 4OH^- \rightarrow O_2 + 2H_2O + 4e^-$$

$$\text{Cathode: } 4H_2O + 4e^- \rightarrow 2H_2 + 4OH^-$$

$$\text{Overall reaction: } 2H_2O \rightarrow 2H_2 + O_2$$

Water molecules react with electrons at the cathode, causing a hydrogen evolution reaction. Hydroxide ions are electrolyzed at the anode to generate oxygen. [44)]

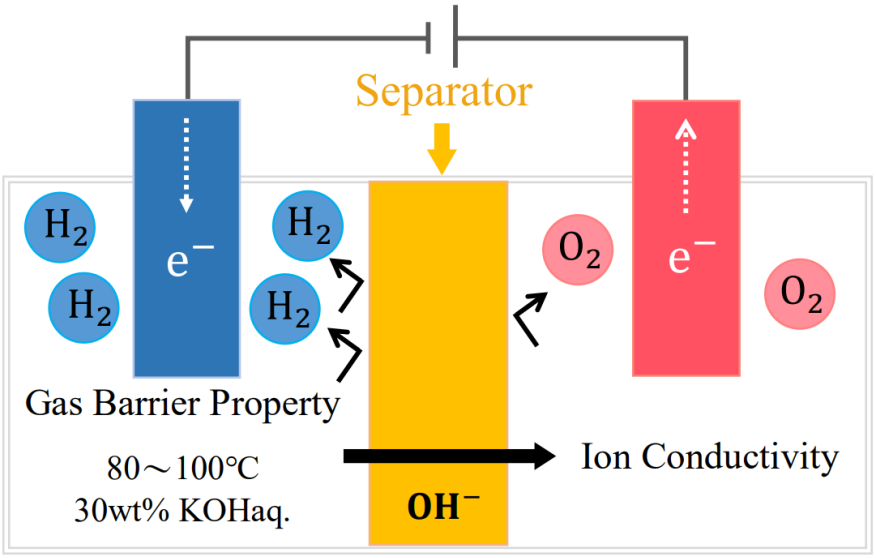

Fig. 1.2 Schematic diagram of water electrolysis cell.

1.2.2 Alkaline Water Electrolysis (AWE) Cells

Hydrogen production by alkaline electrolyzer is a mature technology. The alkaline electrolyzer is safe and reliable, with a service life of up to 15 years, and has been widely used commercially. The working efficiency of an alkaline electrolyzer is generally 42~78%. [45)]

Fig. 1.2 shows a schematic diagram of a general alkaline water electrolyzer. Two sides are the anode and the cathode. The middle is an exchange membrane (separator) with selectively permeating hydroxide ions, sandwiching between the cathode and anode to prevent the mixing of hydrogen and oxygen. At the same time, hydroxide ions at the cathode move through the electrolyte membrane to the anode. The gases exit through channels in the bipolar plates.

Alkaline solutions of 20~30% KOH are usually used in AWE systems. Large electrodes can be manufactured cheaply due to their simple structure. Toshiba Corp. is developing a sizeable AWE production device in Japan. Asahi Kasei Corp. installed

and operated alkaline water electrolysis equipment using large electrodes. [46)]

1.2.3 Electrode Used for the Anodic Reaction for AWE

On the cathode side, platinum (Pt) and its alloys are considered to be the most active HER catalysts. Due to the rare reserves of Pt, many advanced alternative materials have also been proposed. For example, Mo-Co metal compounds also perform well as cathode materials. [47-50)]

The oxygen evolution reaction (OER) process in electrochemical water splitting, including multiple proton/electron processes, is complicated. These processes need to cross a significant energy barrier. All these lead to a high overpotential for the OER reaction. The short-plate effect of the specific processes with the highest overpotential will slow the overall electrochemical water-splitting efficiency. Therefore, compared to HER, OER is kinetically inert in transporting four electrons, which requires high overvoltage. In other words, the rate at which hydrogen is obtained usually depends on the catalytic activity of the anode electrode. [51-54)] As the anode catalyst, Ru/Ir series catalysts are used. Specifically, the oxides of Ir, Rh, Pd, or multiple composite catalysts were applied. Among them, IrO_2 is an electrode material with outstanding oxygen evolution activity, which is the most suitable electrocatalyst for water electrolysis. These electrodes are fabricated by depositing mixed or composite oxides of platinum group metals (such as Ir and Ru) and valve metals (such as Ti and Ta) on porous Ti by pyrolysis. However, scarce storage and high cost limit their large-scale application. [55-58)] Therefore, there is an urgent need to develop cheaper catalysts with high activity, efficiency, and stability. The research topic of this paper is to develop highly active and stable anode materials based on cheap metals.

For the first time, transition group metals were found to possess outstanding catalytic properties and can be exploited at low cost due to their abundance. In recent years, the preparation of OER electrocatalysts utilizing earth-abundant elements has been intensively studied. Among them, nickel oxide-based and cobalt-based alloys

represented by binary alloys and (oxy)hydroxides (e.g., NiFe, NiCo, CoFe) are emerging as the most promising candidates. Moreover, studies have shown that catalysts' composition and surface electronic structure are closely related to their activity. Recently, the introduction of an appropriate third metal species in NiFe-based or CoFe-based (hydroxyl) hydroxides was proved to have a positive effect on further enhancing the OER activity. For example, through combinatorial screening of more than 3,000 trimetallic metal oxides, it was concluded that the most active OER catalysts under alkaline conditions are oxides containing nickel, iron, and other metal species. Based on theoretical calculations, it is believed that the incorporation of tungsten into NiFe-based (hydroxyl) hydroxides can lead to a near-optimized ΔG of the intermediates in the OER process. Ternary NiCoFe(oxy)hydroxides have also proven to be promising for OER. Despite significant progress, further improvement and tuning of catalytic activity are still urgently needed. [59-62)] In addition, catalytic durability is another essential factor to be considered. Because most transition metal-based catalysts perform poorly in terms of stability, the industrialization of catalysts is challenging. [63-64)] From the perspective of development trends, one way to adjust the catalytic activity is to increase the chemical complexity of the catalyst. Among them, the complication of the ingredients is an effective method. [65-66)] When there are five or more constituent elements, this type of material is given a new name, called high-entropy alloy material (HEAM). [67)]

1.3 Review of High-Entropy Alloys (HEAs)

The first investigated metallic high-entropy materials (HEM) are the high-entropy alloys (HEA), which are also called multi-component alloys, complex composition alloys (CCA), and base-free alloys (BA). [68-69)] Since the first publication in 2004, it has received extensive attention and research from scientists. Cantor showed his interest in preparing multi-principal alloys in the 1970s, compared to the fact that traditional materials use a single primary element and add other trace alloying

elements to regulate the final properties. For traditional materials, adding ppm-level B elements in steel can improve grain boundary strengthening, and adding 1% or 2% Re in superalloys can increase the temperature-bearing capacity by several degrees. The new HEA, in a multi-principal manner, provides many possibilities for exploring unusual new materials. In 1979, Cantor prepared an equiatomic ratio alloy containing 20 elements by heating, melting, water cooling, and solidification. This equiatomic ratio alloy is composed of several complex phase structures, as shown in Fig. 1.3. Analysis revealed that one of the FCC single phases is composed of 5 equal proportions of Cr, Mn, Fe, Co, and Ni. After 20 years of unremitting efforts, this result was first presented at the RQ11 conference (Oxford) in 2002 and finally published in the Journal of Materials Science and Engineering in 2004. This alloy is the widely studied multi-principal single-phase Cantor alloy CrMnFeCoNi. [70)]

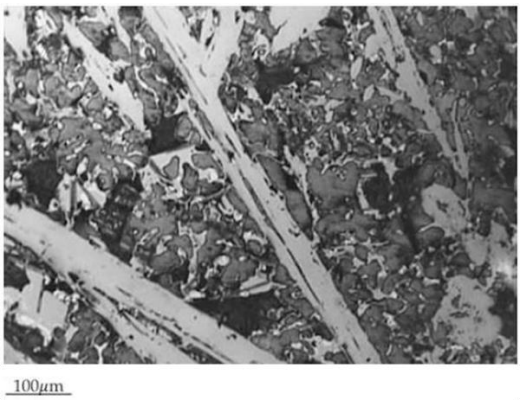

Fig.1.3 Optical micrograph of the multi-phase microstructure of MgAlSiMnCrFeCoNiCuZnGeNbMoAgCdSnSbWPbBi alloy. [70)]

1.3.1 Definition of HEAs

Although there is no general definition of HEAs, the theoretical concept of entropy is recognized for their high stability. Entropy is a thermodynamic state function, and the essence of entropy is the "inner chaos" of the system. According to the statistical principle of Boltzmann thermodynamics, the quantitative relationship between the

entropy and randomness of the system is given by the following equation (1.1).

$$\Delta S_{conf} = k \ln \omega \ldots\ldots (1.1)$$

where k is the Boltzmann constant and w is the number of atom configuration possibilities. The total mixing entropy includes configurational entropy (ΔS_{mix}^{conf}), vibrational entropy (ΔS_{mix}^{vib}), magnetic dipole entropy (ΔS_{mix}^{elec}), electronic randomness entropy (ΔS_{mix}^{mag}), and the interaction between them. Four contribute and are given by equation (1.2).

$$\Delta S_{mix} = \Delta S_{mix}^{conf} + \Delta S_{mix}^{vib} + \Delta S_{mix}^{elec} + \Delta S_{mix}^{mag} \ldots\ldots (1.2)$$

The configuration entropy is dominant compared to the other three entropies. Therefore, the configuration entropy avoids complex calculations to determine the other three contributions and can approximately represent the mixed entropy. For an ideal random n-component solid solution, the ideal configure ational entropy per mole is given by Eq. 1.3. [71)]

$$\Delta S_{conf} = -R\ (c_1 \ln c_1 + c_2 \ln c_2 + \ldots + c_n \ln c_n)$$

$$= -R \sum_{i=1}^{n} c_i \ln c_i \ldots\ldots (1.3)$$

where R is the gas constant, c_i is the mole fraction of the ith element, and n is the number of components. According to the extremum theorem, the system's entropy reaches a maximum when $c_1 = c_2 = \ldots = c_n$. HEAs are said to have a random-state configuration entropy greater than 1.5R, regardless of whether they are single-phase or multi-phase at room temperature. Although the above definitions are widely accepted, quaternary equimolar alloys are sometimes considered HEAs in the literature because their composition and configurational entropy are near the lower bounds of both definitions. Therefore, the definition of HEA is only a rough guideline and not a hard and fast rule. [72)]

1.3.2 Developed HEAs

As introduced in Section 1.3.1, alloys containing five or more principal elements in a single solid solution phase are often called high-entropy alloys (HEAs). The generally accepted definition is that the constituent elements in high-entropy alloys are composed of equal or nearly equal atomic ratios, and the content of each element is between 5% and 35%. [73)] Moreover, they exhibit unusual physicochemical and mechanical properties, such as enhanced strength, stability, and corrosion resistance, distinguishing them from heterogeneous intermetallic alloys. [74-76)] As research progresses, possible root causes include high-entropy effects in thermodynamics, lattice distortion effects in structure, delayed diffusion effects in kinetics, and cocktail effects in performance. [77)] These characteristics make high-entropy alloys have high strength, wear resistance, and excellent corrosion resistance. [78)] For example, the most representative CrMnFeCoNi alloy exhibits excellent low-temperature toughness. This alloy exhibits high fracture toughness at liquid nitrogen temperatures (approximately -196°C). Compared with traditional alloys, such as ordinary metal materials and iron and steel materials, when cooled below room temperature, the plasticity, and toughness of the steel material decrease significantly under stress loading, causing severe brittle fracture. However, high-entropy alloys (CrMnFeCoNi) overcome this problem and have a significant breakthrough. [79)]

On the other hand, due to the lattice distortion effect of the high-entropy alloy, more microscopic defects are formed, and the more stable solid solution structure formed by the high-entropy effect endows the material with superior catalytic performance and stability. [80)] Furthermore, the catalyst performance is also enhanced by the inherent surface complexity of HEA, which can provide a near-continuous distribution of adsorption energy across surface sites and maximize the proportion of optimal active sites. This sets the stage for potential catalytic performance. [81)] In conclusion, HEAs can be considered promising catalyst candidates for OER. From the existing research, the OER performance of some HEAs exhibited better activity than the currently commercialized iridium dioxide and ruthenium dioxide. [82)]

1.4 Review of High-Entropy Oxides (HEOs)

High-entropy materials (HEMs) are not limited to alloys; high-entropy alloy compounds have gradually come into our eyes, among which are representative high-entropy alloy carbides, nitrides, phosphides, sulfides and oxides. High-entropy alloy oxides (HEOs) have been the most studied as anode catalyst materials for water electrolysis. For example, Nguyen et al. prepared optimized $La(CrMnFeCo_2Ni)O_3$ perovskite HEOs (L_5M_2Co) with an extra high Co^{3+}/Co^{2+} ratio. [83] They achieved an excellent 325 mV OER overpotential at a current density of 10 mA/cm^2 and super-electrochemical stability after 50 h. Moreover, they found that doubling the Co was the most effective to increase the OER activity among the above-influencing factors. Except for element influence, the overall shape of HEOs is also designed to perfect the electrocatalytic performances. Porous nanostructures have become particularly attractive because of their enormous specific surface area which can provide more active contact sites to increase the OER activity. [84]

High-entropy oxides (HEO) are inherited from high-entropy alloys and have aroused widespread interest among scientists. The unique characteristics of the new high-entropy oxide as an electrode material meet the following characteristics: (1) The high-entropy effect of HEOs can increase the solid solution limit between elements and provide stability for the generated random solid solution, which is of great significance. [85] (2) The slow diffusion effect that hinders the growth of the second-phase nanostructure can ensure the stability of the electrode when the operating temperature changes. [86] (3) Severe lattice distortion is conducive to the strengthening and hardening of materials. Although the thermal and electrical conductivity of HEOs will be reduced, it will significantly enhance the material's pressure resistance and reduce the lattice's expansion and contraction and the generation of defects to ensure the stability and safety of the electrode material after charge and discharge cycles. [87] (4) The cocktail effect can provide the magical properties of a mixture of multiple elements to increase the material's functionality. For these reasons, many recent studies have shown that high-entropy oxides have great electrochemistry potential. [88]

In recent years, the burgeoning demand for hydrogen energy has prompted a remarkable surge in advanced electrochemical technology concerning HEO as an electrode. The design and preparation of HEO emerged as determinants of the properties of new energy conversion and storage technologies. Despite the significant strides made in this domain, there is an urgent need to address the safety properties of HEO, such as durability after numerous charge and discharge cycles, which remain critical challenges to overcome. The unique characteristics of new high-entropy oxide materials are well-suited to address the demands mentioned above. [89)]

1.4.1 Synthesis Method and Crystal Structure of HEOs

Synthetic methods and operating conditions are crucial to the thermodynamic or kinetic factors affecting the preparation of high-entropy oxides with a single solid solution phase. In recent studies, most high-entropy oxides have been prepared by classical high-temperature solid-state reactions between metal salts because of their ease of handling. The usual preparation process is: (1) Metal oxides are mixed mechanically by ball milling to obtain a homogeneous powder; (2) The powders are dried and pre-fired to form the main crystalline phase; (3) Secondary grinding and granulation of high entropy oxide particles; (4) The granules are screened and dry-pressed; (5) Finally, perform high-temperature quenching. In addition to the above methods, other methods for preparing metal oxide mixtures can also be used to prepare high-entropy oxides, such as co-precipitation, solvothermal, hydrothermal, mechanochemical, sonochemical, solution combustion, spray pyrolysis, and chemical reduction. The actual demand and the purpose of preparation affect the choice of preparation method to a certain extent. For example, co-precipitation is more favorable for large-scale preparation. The shape of the HEOs can also affect experimental results. Therefore, more complicated processes are usually used to prepare HEOs based on the above method in practical research. However, the abovementioned methods are cumbersome, and most require high-temperature or

high-pressure treatments. This means that there are specific requirements for the equipment. Moreover, nanoparticles can easily agglomerate under high-temperature conditions, so the morphology cannot be well controlled. After the material is obtained again, it is necessary to adhere the material to the surface of the electrode with a binder, in case of being used electrode. The binder will also reduce the conductivity of the electrode material and cannot support a large current. [90)]

Thermal treatment of HEO at different temperatures results in the formation of different phase structures. [91-92)] Typically, there is a specific temperature range within which single-phase entropy stabilization is achieved for a specific metal oxide with multiple compositions. [93)] In contrast, outside of this range, multi-phase mixtures dominate. Moreover, HEO provides a wealth of options for ingredient selection and crystal structure type, allowing for the continuous discovery of new HEOs. [94)]

To date, most research has focused on the synthesis and exploration of properties of entropy-stable oxides based on the seminal work of Rost et al. [95)] HEO with rock salt structure is the most studied and earliest. [95)] Typically, entropy-stable oxides are used to illustrate rock-salt-structured HEOs, which exhibit typical entropy-driven phase stabilization effects. Among them, the typical representative is the synthesized $(MgCoNiCuZn)_{0.2}O$ and its corresponding derivatives, which have received the most attention. [96)] Spinel high entropy oxides $(Ni_{0.2}Co_{0.2}Mn_{0.2}Fe_{0.2}Ti_{0.2})_3O_4$, $(Co_{0.2}Cr_{0.2}Fe_{0.2}Mn_{0.2}Ni_{0.2})_3O_4$ and $(Al_{1/6}Co_{1/6}Cr_{1/6}Fe_{1/6}Mn_{1/6}Ni_{1/6})_3O_4$ has recently been prepared. Its purpose is mainly applied to lithium-ion storage, mainly improving oxygen vacancies. [97-98)] Enabling oxygen vacancies can usually increase the electronic conductivity of O atoms around the oxygen vacancies. It can make up for defects in the initial band structure, while the conduction band will shift to the Fermi level. [99)] In addition, perovskite-structured HEO materials have also been widely used in many fields such as catalysis. Furthermore, research attention has been focused on improving the stability of these materials. Therefore, its design and synthesis become attractive. Unlike other high-entropy oxides, the perovskite structure mainly has two cationic sublattices and is extremely rich in elemental composition. In addition to the design of perovskite compositions, the spatial structure of perovskites has also been

considered in recent years. Layered perovskites, especially perovskite oxide epitaxial films, have become popular research in recent years due to their better environmental stability and structural adjustability than non-layered perovskites. The large specific surface area provides more catalytic sites and is also one of the popular research objects. In addition to the common structures mentioned above, more oxide systems have also been synthesized, such as pyrochlore ($(LaNdSmCeGdEuY)_2Zr_2O_7$) with six cations and scheelite $(Ca_{0.5}Ce_{0.5})(Nb_{0.25}Ta_{0.25}Mo_{0.25}W_{0.25})O_4$. [100-103)]

Contrary to the abovementioned crystal structure, the high-entropy amorphous oxide structure is also a new type of material developed in recent years. However, compared with HEO with a single structure, HEO with an amorphous structure is a complex material in structure and composition, so there are only a handful of related studies. On this basis, the performance of amorphous HEO materials as OER electrode materials, their stability during long-term testing, and the impact of amorphous are worthy of attention. Also, based on HEO, amorphous has the advantages of eliminating the rich and poor differentiation of elements within the material and the potential differences in different regions, reducing the probability of pitting corrosion, delaying the corrosion rate, and improving stability. Moreover, the surface has highly active sites for chemical reactions, which is conducive to the rapid progress of oxygen-catalytic reactions. [104-106)]

Compared to the above others, the preparation of HEO materials by electrodeposition is a research topic with extraordinary potential because electrodeposition mainly has the following two advantages: (1) It does not require high temperature and high-pressure conditions, has low requirements on equipment, and is easy to operate; (2) Directly attached, not limited by electrode shape and shape, no adhesive required.

1.4.2 HEAs Synthesis by Electrodeposition

Electrodeposition (electrochemical deposition or plating) can deposit HEA films on complex-shaped substrates and can be performed at low processing temperatures and low energy consumption. Electrodeposition has the potential for low-cost synthesis of HEA films because it does not require complex equipment or large amounts of raw materials. Furthermore, the electrodeposition parameters can be controlled by changing the composition, morphology, and thickness of the electrodeposited film. The thin film research related to such electrodeposition is summarized as follows.

1) Yao et al. prepared BiFeCoNiMn, TmFeCoNiMn, MgMnFeCoNiGd, and FeNiCoBiMn films for the first time in organic solutions. The film composition, structure, and magnetic characteristics were studied. [107-110)]

2) Soare V et al. also synthesized AlCrFeMnNi and AlCrCuFeMnNi high-entropy alloy films in organic solutions and characterized the microstructure. [111)]

3) Ionut Constantin et al. used pulse electrodeposition method to synthesize CoCrFeMnNi high-entropy alloy films for the first time, and studied the composition changes by changing pulse conditions. [112)]

It can be seen that the research on the synthesis of high-entropy alloy thin films by electrodeposition is only in its infancy.

1.5 Futural Issues and Purpose of this Thesis

According to the above-described background, it is essential to solve the following issues for constructing the hydrogen society both in practical application and academic investigation: (1) Exploring novel catalyst materials with complex components and structures to achieve high catalytic activity and stable/long life for OER, and (2) Developing simple and low-cost synthesis method of the catalytic electrode for large scale applications in water electrolysis.

As a resolution to solve the above problems and a challenge to explore novel

materials used for OER in water electrolysis, this study proposed the base elements of the oxygen-containing film as the transition elements of Cr, Mn, Fe, Co, and Ni. A simple one-step electrodeposition method was developed in organic solvent. The catalytic performance was clarified on the prepared electrodes. Using the anhydrous organic solvents has several advantages: (1) The H_2 evolution, which consumes much electricity, can be avoided; (2) Potentials can be freely applied to control film formation rate, composition, and microstructure. An amorphous film can be obtained in the solution. This amorphization is expected, leading to the disordered arrangement of atoms in the film, thus exposing multiple active metal sites to accelerate the OER reaction.

1.6 Structure of this Thesis

This thesis comprises 4 chapters, including an introduction (Chapter 1) and a summary (Chapter 4).

In Chapter 2, it was revealed that the supporting electrolyte $LiClO_4$ in organic solvent is not conducive to the formation of stable films at a given deposition potential. On this basis, a bath solution without using $LiClO_4$ was constructed, and an oxygen-containing CrMnFeCoNi film was synthesized on a copper substrate. In addition, the composition and crystal structure of the obtained film were studied. In In Chapter 3, the effects of the presence or absence of supporting electrolytes in organic solvents and various electrodeposition potentials on the composition, crystal structure, and chemical bonding state of the films are elucidated. Furthermore, the conditions for the synthesis of oxygen-containing CrMnFeCoNi films on copper substrates without using a $LiClO_4$ bath were determined and the deposition mechanism was discussed. Finally, the films were applied as anodic electrodes for oxygen evolution reaction (OER) in water electrolysis, and the catalytic activity was measured. In this way, a one-step method for preparing oxygen-containing CrMnFeCoNi films without the use of supporting electrolytes was established. Furthermore, the oxygen-

containing CrMnFeCoNi film was used to OER electrode for water electrolysis and confirmed its high catalytic activity.

References

1) K. Jaiswal, C. Chowdhury, D. Yadav, R. Verma, S. Dutta, K. Jaiswal, S. B, Ka. Karuppasamy; Energy Nexus; 7, 100118, 2022.

2) A. Awan; International Journal of Asian Social Science; 3, 741-761, 2013.

3) V. Arutyunov, G. Lisichkin; Russian Chemical Reviews; 86, 777, 2017.

4) J. Sachs, R. Cooper, S. Fischer; Brookings Papers on Economic Activity; 1981, 201-282, 1981.

5) W. Broecker; Science; 189, 460-463, 1975.

6) P. Epstein; Scientific American; 283, 50-57, 2000.

7) A. Khasnis, M. Nettleman; Archives of Medical Research; 36, 689-696, 2005.

8) K. Abbass, M. Qasim, H. Song, M. Murshed, H. Mahmood, I. Younis; Environmental Science and Pollution Research; 29, 42539-42559, 2022.

9) M. Yamamoto, Focus NEDO, 52, 7, 2014.

10) J. Rogelj, O. Geden, A. Cowie, A. Reisinger; Comment; 591, 365-368, 2021.

11) S. Pye, F. Li, J. Price, B. Fais; Nature Energy; 2, 17024, 2017.

12) H. Soest, M. Elzen, D. Vuuren; Nature Communications; 12, 2140, 2021.

13) O. Anika, S. Nnabuife, A. Bello, E. Okoroafor, B. Kuang, R. Villa; Carbon Capture Science & Technology; 5, 100072, 2022.

14) I. Karlsson, J. Rootzén, F. Johnsson; Renewable and Sustainable Energy Reviews; 120, 109651, 2020.

15) E. Dogan, M. Madaleno, D. Taskin, P. Tzeremes; Renewable Energy; 197, 709-722, 2022.

16) N. Stepaniuk; Nationalities Papers; 82, 1-18, 2022.

17) A. Sarker, A. Azad, M. Rasul, A. Doppalapudi; Energies; 16, 16031556, 2023.

18) A. Nemmour, A. Inayat, I. Janajreh, C. Ghenai; International Journal of Hydrogen

Energy; 48, 29011-29033, 2023.

19) F. Dawood, M. Anda, G. Shafiullah; International Journal of Hydrogen Energy; 45, 3847-3869, 2020.

20) G. Marbán, T. Solís; International Journal of Hydrogen Energy; 32, 1625-1637, 2007.

21) Mary Elvira Weeks; Chemical Education; 9, 215, 1932.

22) M. Schoell; Geochimica et Cosmochimica Acta; 44, 649-661, 1980.

23) S. Ahmed, M. Krumpelt; International Journal of Hydrogen Energy; 26, 291-301, 2001.

24) K. Santos, C. Eckert, E. Rossi, R. Bariccatti, E. Frigo, C. Lindino, H. Alves; Renewable and Sustainable Energy Reviews; 68, 563-571, 2017.

25) K. Nassau; Azimuth; 1, 123-168, 1998.

26) J. Arcos, D. Santos; Gases; 3, 3010002, 2023.

27) M. Steilen, L. Jörissen; Electrochemical Energy Storage for Renewable Sources and Grid Balancing; 143-158, 2015.

28) P. Puranen, A. Kosonen, J. Ahola; Solar Energy; 213, 246-259, 2021.

29) D. Gielen, E. Taibi, R. Miranda; Hydrogen Knowledge Centre; 2019.

30) Jaeryoung, Kim Cheolhu, Yang Rywon, Yoon, Sung; The International Journal of Climate Change: Impacts and Responses; 15, 47-68, 2023.

31) M. Huang, P. Zhai; Advances in Climate Change Research; 12, 281-286, 2021.

32) R. Wüstenhagen, M. Bilharz; Energy Policy; 34, 1681-1696, 2006.

33) H. Matsubara; Institute for Sustainable Energy Policies 2018; 2018.

34) Y. Matsuo, S. Endo, Y. Nagatomi, Y. Shibata, R. Komiyama, Y. Fujii; Energy; 165, 1200-1219, 2018.

35) R. Felseghi, E. Carcadea, M. Raboaca, C. TRUFIN, C. Filote; Energies; 12, 12234593, 2019.

36) L. Fan, Z. Tu, S. Chan; Energy Reports; 7, 8421-8446, 2021.

37) M. Sterner, M.Specht; Energies; 14, 14206594, 2021.

38) M. McPherson, N. Johnson, M. Strubegger; Applied Energy; 216, 649-661, 2018.

39) S. Sebbahi, N. Nabil, A. Belghiti, S. Laasri, S. Rachidi, A. Hajjaji; Materials

Today: Proceedings; 66, 140-145, 2022.

40) S. Grigoriev, V. Fateev, D. Bessarabov, P. Millet; International Journal of Hydrogen Energy; 45, 26036-26058, 2020.

41) R. Gao, L. Zhang, L. Wang, X. Zhang, C. Zhang, K. Jun, S. Kim, H. Park, Y. Gao, Y. Zhu, T. Zhao, H. Wan, G. Guan; Energy Conversion and Management; 263, 115671, 2022.

42) D. Jang, J. Kim, D. Kim, W. Han, S. Kang; Energy Conversion and Management; 258, 115499, 2022.

43) S. Kumar, V. Himabindu; Materials Science for Energy Technologies; 2, 442-454, 2019.

44) Y. Feng, X. Li, Q. Liu, W. Zhu, X. Huo, M. Gao, W. Liu, Y. Wang, Y. Wei; Materials Chemistry Frontiers; 7, 6446-6462, 2023.

45) L. Gandía, R. Oroz, A. Ursúa, P. Sanchis, P. Diéguez; Energy Fuels; 21, 1699-1706, 2007.

46) Y. Nakajima, N. Fujimoto, S. Hasegawa, T. Usui; ECS Transactions; 80, 10, 2017.

47) X. Yu, S. Ye; Journal of Power Sources; 172, 145-154, 2007.

48) E. Antolini, J. Salgado, E. Gonzalez; Journal of Power Sources; 160, 957-968, 2006.

49) H. Gasteiger, S. Kocha, B. Sompalli, F. Wagner; Applied Catalysis B: Environmental; 56, 9-35, 2005.

50) L. Pan, S. Ott, F. Dionigi, P. Strasser; Current Opinion in Electrochemistry; 18, 61-71, 2019.

51) R. Chen, C. Yang, W. Cai, H. Wang, J. Miao, L. Zhang, S. Chen, B. Liu; ACS Energy Letters; 2, 1070-1075, 2017.

52) S. Fajardo, G. Frankel; Electrochimica Acta; 165, 255-267, 2015.

53) L. Gu, N. Luo, G. Miley; Journal of Power Sources; 173,77-85, 2007.

54) C. Lamy, T. Jaubert, S. Baranton, C. Coutanceau; Journal of Power Sources; 245, 927-936, 2014.

55) L. Wang, V. Saveleva, S. Zafeiratos, E. Savinova, P. Lettenmeier, P. Gazdzicki, A. Gago, K. Friedrich; Nano Energy; 34, 385-391, 2017.

56) T. Reier, M. Oezaslan, P. Strasser; ACS Catalysis; 2, 1765-1772, 2012.

57) M. Reis, A. Neto, V. Vasconcelos, A. Dória, G. Santos, E. Santos, K. Eguiluz, G. Banda; Journal of Electroanalytical Chemistry; 895, 115461, 2021.

58) K. Koko, E. Mayousse, T. Napporn, K. Servat, N. Guillet, E. Soyez, A. Grosjean, A. Rakotondrainibé, J. Paul-Joseph; International Journal of Hydrogen Energy; 39, 1924-1931, 2014.

59) D. Wang, D. Astruc; Chemical Society Reviews; 46, 816-854, 2017.

60) B. Su, Z. Cao, Z. Shi; ACS Accounts of Chemical Research; 48, 886-896, 2015.

61) J. Obligacion, P. Chirik; Nature Reviews Chemistry; 2, 15-34, 2018.

62) H. Osgood, S. Devaguptapu, H. Xu, J. Cho, G. Wu; Nanotoday; 11,601-625, 2016.

63) M. Monai, M. Melchionna, P. Fornasiero; Advances in Catalysis; 63,1-73, 2018.

64) X. Li, C. Huang, W. Han, T. Ouyang, Z. Liu; Chinese Chemical Letters; 32, 2597-2616, 2021.

65) P. Munnik, P. Jongh, K. Jong; ACS Chemical Reviews; 14, 6687-6718, 2015.

66) H. Cong, J. Porco, Jr.; ACS Catalysis; 2, 65-70, 2012.

67) H. Liu, L. Syama, L. Zhang, C. Lee, C. Liu, Z. Dai, Q. Yan; Wiley Online Library; 1, 482-505, 2021.

68) R. Ezzat, E. Sara; Current Organic Chemistry; 21, 752-778, 2017.

69) Z. He, G. Wang, C. Wang, L. Guo, R. Wei, G. Song, D. Pan, R. Das, N. Naik, Z. Hu, Z. Guo; Polymer Reviews; 61, 689-713, 2020.

70) Brechtl J, Liaw P K. High-Entropy Materials: Theory, Experiments, and Applications; Springer; 2021.

71) Miracle D, Senkov O; Acta Materialia; 122, 448-551, 2017.

72) J. Yeh; The Journal of The Minerals, Metals & Materials Society (TMS); 65, 1759-1771, 2013.

73) L. Santodonato, Y. Zhang, M. Feygenson, C. Parish, M. Gao, R. Weber, J. Neuefeind, Z. Tang, P. Liaw; Nature Communications; 6, 5964, 2015.

74) A. Sharma, S. Yadav, K. Biswas, B. Basu; Materials Science and Engineering: R: Reports; 131, 1-42, 2018.

75) I. Hussain, C. Lamiel, M. Ahmad, Y. Chen, S. Shuang, M. Javed, Y. Yang, K.

Zhang; Journal of Energy Storage; 44, 103405, 2021.

76) R. Nutor, Q. Cao, X. Wang, D. Zhang, Y. Fang, Y. Zhang, J. Jiang; Advanced Engineering Materials; 22, 2000466, 2020.

77) B. Wang, Y. Yao, X. Yu, C. Wang, C. Wu, Z. Zou; J. Mater. Chem. A.; 9, 19410-19438, 2021.

78) N. Hua, W. Wang, Q. Wang, Y. Ye, S. Lin, L. Zhang, Q. Guo, J. Brechtl, P. Liaw; Journal of Alloys and Compounds; 861, 157997, 2021.

79) K. Ming, W. Lu, Z. Li, X. Bi, J. Wang; Acta Materialia; 188, 354-365, 2020.

80) G. Tomboc, T. Kwon, J. Joo, K. Lee; Journal of Materials Chemistry A; 8, 14844-14862, 2020.

81) L. Yu, K. Zeng, C. Li, X. Lin, H. Liu, W. Shi, H. Qiu, Y. Yuan, Y. Yao; Carbon Energy; 4, 731-761, 2022.

82) L. Li, X. Cao, J. Huo, J. Qu, W. Chen, C. Liu, Y. Zhao, H. Liu, G. Wang; Journal of Energy Chemistry; 76, 195-213, 2023.

83) T. Nguyen, Y. Liao, C. Lin, Y. Su, J. Ting; Advanced Functional Materials; 31, 2101632, 2021.

84) H. Xu, H. Shang, C. Wang, Y. Du; Advanced Functional Materials; 30, 2006317, 2020.

85) S. McCormack, A. Navrotsky; Acta Materialia; 202, 1-21, 2021.

86) G. Korotcenkov, B. Cho; Sensors and Actuators B: Chemical; 156, 527-538, 2011.

87) L. Li, Q. Fang, J. Li, B. Liu, Y. Liu, P. Liaw; Materials Science and Engineering: A; 784, 139323, 2020.

88) Y. Gao, L. Yu, J. Yeo, C. Lim; Advanced Materials; 32, 1902133, 2019.

89) Z. Lun, B. Ouyang, D. Kwon, Y. Ha, E. Foley, T. Huang, Z. Cai, H. Kim, M. Balasubramanian, Y. Sun, J. Huang, Y. Tian, H. Kim, B. McCloskey, W. Yang, R. Clément, H. Ji, G. Ceder; Nature Materials; 20, 214-221, 2021.

90) S. Aamlid, M. Oudah, J. Rottler, A. Hallas; Journal of the American Chemical Society; 145, 5991-6006, 2023.

91) Y. Park, S. Moon, J. He; Ceramics International; 29, 223-227, 2003.

92) M. Park, C. Choi, W. Lim, M. Kim, J. Choi, N. Heo; Microporous and

Mesoporous Materials; 37, 81-89, 2000.

93) A. Sarkar, R. Djenadic, N. Usharani, K. Sanghvi, V. Chakravadhanula, A. Gandhi, H. Hahn, S. Bhattacharya; Journal of the European Ceramic Society; 37, 747-754, 2017.

94) X. Liu, H. Wang, L. Dong, K. Li, H. Zhang, Q. Jia, S. Zhang, W. Lei; Journal of Energy Chemistry; 86, 536-545, 2023.

95) X. Zou, Y. Zhang, Z. Huang, K. Yue, Z. Guo; Chemical Communications; 59, 13535-13550, 2023.

96) W. Mnasri, D. Bérardan, S. Nenez, T. Gacoin, I. Maurin, N. Dragoe; J. Mater. Chem. C; 9, 15121-15131, 2021.

97) T. Chen, S. Wang, C. Kuo, S. Huang, M. Lin, C. Li, H. Chen, C. Wang, Y. Liao, C. Lin, Y. Chang, J. Yeh, S. Lin, T. Chen, H. Chen; J. Mater. Chem. A; 8, 21756-21770, 2020.

98) A. Sarkar, B. Eggert, R. Witte, J. Lill, L. Velasco, Q. Wang, J. Sonar, K. Ollefs, S. Bhattacharya, R. Brand, H. Wende, F. Groot, O. Clemens, H. Hahn, R. Kruk; Acta Materialia; 226, 117581, 2022.

99) K. Ye, K. Li, Y. Lu, Z. Guo, N. Ni, H. Liu, Y. Huang, H. Ji, P. Wang; TrAC Trends in Analytical Chemistry; 116, 102-108, 2019.

100) Z. Sun, Y. Zhao, C. Sun, Q. Ni, C. Wang, H. Jin; Chemical Engineering Journal; 431, 133448, 2022.

101) Z. Zheng, H. Ji, Y. Zhang, J. Cai, C. Mo; Solid State Ionics; 377, 115872, 2022.

102) X. Wang, X. Li, H. Fan, M. Miao, Y. Zhang, W. Guo, Y. Fu; Journal of Energy Chemistry; 67, 276-289, 2022.

103) M. Haque, A. Sheikh, X. Guan, T. Wu; Advanced Energy Materials; 7, 1602803, 2017.

104) Y. Ma, Y. Ma, Q. Wang, S. Schweidler, M. Botro, T. Fu, H. Hahn, T. Brezesinski, B. Breitung; Energy Environ. Sci.; 14, 2883-2905, 2021.

105) J. Lin, R. Reddy, C. Zeng, X. Lin, A. Zeb, C. Su; Coordination Chemistry Reviews; 446, 214118, 2021.

106) K. Huang, Y. Sun, Y. Zhang, X. Wang, W. Zhang, S. Feng; Advanced Materials;

31, 1801430, 2018.

107) C. Yao, P. Zhang, M. Liu, G. Li, J. Ye, P. Liu, Y. Tong; Electrochimica Acta; 53, 8359–8365, 2008.

108) C. Yao, P. Zhang, M. Liu, G. Li, J. Ye, P. Liu, Y. Tong; J. Rare Earth; 29, 133-137, 2011.

109) H. Li, H. Sun, C. Wang, B. Wei, C. Yao, Y. Tong, H. Ma; J. Alloy Compd.; 598, 161-165, 2014.

110) M. Zheng, Y. Li, J. Hu, Y. Zhao; MSAIJ; 11, 344-348, 2014.

111) V. Soare, M. Burada, I. Constantin, D. Mitrică, V. Bădiliţă, A. Caragea, M. Târcolea; Appl. Surf. Sci.; 358, 533-539, 2015.

112) F. Yoosefan, A. Ashrafi, S. vaghefi. I. Constantin; Metals and Materials International; 26,1262–1269, 2020.

Chapter 2 Influence of Supporting Electrolyte $LiClO_4$ on the Synthesis of Oxygen-Containing CrMnFeCoNi Film by Electrodeposition in an Organic Solvent

2.1 Introduction

High-entropy alloys are solid solutions consisting of multi metal elements in near equal atomic ratios. [1-3] Usually, intermetallic compounds with a certain particular element ratio are suppressed in these alloys. On the other hand, nanoscale precipitates can be utilized to improve strength. [4-9] Many high-entropy alloys have high-temperature strength, low-temperature ductility, excellent corrosion resistance, high-temperature stability, and electromagnetic properties. Therefore, many industrial applications are expected. [10-16] Much attention, as next-generation structural materials, tool materials, corrosion-resistant materials, electromagnetic materials, high/low temperature materials, catalyst materials, etc. are attracted. [17] Constituent elements of high-entropy alloys are generally selected from Al, Ti, V, Cr, Mn, Fe, Co, Ni, Cu, Zn, Mo, W, Nb, Sn, Hf, Ta, Pb, Si, B, etc. As processing methods, bulk alloys are formed by vacuum melting, powder metallurgy, mechanical alloying, laser melting, etc., [2, 18-20] and films are formed by thermal spraying, magnetron sputtering, laser cladding, electrodeposition, etc. [2, 20-24] These alloys can be further subjected to heat treatment to control their structure and improve their functionality. [8, 9, 25]

When utilizing the surface features of high-entropy alloys, such as corrosion resistance, wear resistance, catalytic activity, and electromagnetic properties, it is

more advantageous to fabricate alloy thin films than bulk alloys from the viewpoint of resource conservation and weight reduction. When producing thin alloy films, electrodeposition can be carried out at lower temperatures than thermal spraying or magnetron sputtering. It can be coated on substrates with complex shapes and is also suitable for the production of nanomaterials and amorphous materials. Furthermore, by adjusting the electrodeposition conditions (concentration, temperature, potential, current, time, of the solution), the chemical composition, thickness, and structure of the film can be controlled.

In addition, in consideration of the applicable range of electrodeposition potential and improvement of electrodeposition efficiency, it is desirable to use an anhydrous salt organic solvent solution instead of the aqueous solution.

However, in complex solutions containing various types of salts, the redox potential of metal ions may change significantly due to interactions between ions and the formation of complex compounds. [16, 26)] Therefore, it is not easy to incorporate many types of elements in the same atomic ratio into the film. Until now, it has been considered effective to add a supporting electrolyte, $LiClO_4$, to a solvent such as DMF (dimethylformamide), CH_3CN (acetonitrile), or DMSO (dimethyl sulfoxide) for the production of high-entropy alloy films. [14-16, 27-30)] Preliminary experiments were conducted to confirm its effectiveness, and then it was discovered that the film peeled off during cleaning in water. On the other hand, from the above literature, it is not clear how lithium ions (Li^+) in the liquid affect the formation of the film or what the components and composition of the film are. In order to develop high-quality electrodeposited films of high-entropy alloys, it is necessary to investigate the electrodeposition process in a solvent containing Li^+ and to clarify the composition and structure of the formed films.

Here, in this chapter, several electrodeposited films containing CrMnFeCoNi were prepared in the organic solvent DMF-CH_3CN with and without the addition of supporting electrolyte $LiClO_4$. In addition, various analytical methods were used to investigate the effects of the supporting electrolyte on the surface morphology, components, and crystal structure of the film. Finally, the formation process of the

deposited film was investigated based on the film structure obtained.

2.2 Experimental

A dephosphorylated copper plate (99.93 mass%) polished by #2000 emery paper was ultrasonically cleaned in acetone, dried with hot air, and used as a substrate for electrodeposition. Before electrodeposition, the substrate was degreased and neutralized in a sequence of 10% sodium hydroxide (NaOH) and 10% hydrochloric acid (HCl) aqueous solution. An insulating tape was pasted on the back surface, and a copper lead wire was drawn. The solutions were the organic solvent DMF(C_3H_7NO)-CH_3CN (volume ratio 4:1) of solution A without the supporting electrolyte $LiClO_4$ and solution B with 0.1 M $LiClO_4$. Chemicals of $CrCl_3$•$6H_2O$, $MnCl_2$, $FeCl_2$•$4H_2O$, $CoCl_2$ and $NiCl_2$•$6H_2O$ were sequentially dissolved therein. After that, in order to remove the moisture brought by the organic solvent and the chemicals, the solution was dehydrated for 24 hours using molecular sieves 4A ($Na_{12}[(AlO_2)_{12}(SiO_2)_{12}]$・$27H_2O$) (1/16, Fuji Film Wako Pure Chemical Industries, Ltd.). Table 1 shows the concentrations of $CrCl_3$, $MnCl_2$, $FeCl_2$, $CoCl_2$, $NiCl_2$, and $LiClO_4$ used to prepare solution A and solution B. These two types of solutions were selected based on the results of preliminary experiments in order to make the film contain Cr, Mn, Fe, Co and Ni in approximately equal amounts.

Table 1 Solutions for electrodeposition in organic solvent of DMF and CH_3CN (4:1 by volume).

Solution	$CrCl_3$ (M)	$MnCl_2$ (M)	$FeCl_2$ (M)	$CoCl_2$ (M)	$NiCl_2$ (M)	$LiClO_4$ (M)
A	0.06	0.1	0.04	0.06	0.02	-
B	0.01	0.01	0.01	0.01	0.01	0.1

Electrodeposition was performed in a glass breaker containing organic solvent-based solutions at 313 ± 1K after nitrogen deaeration for 1.8ks. The counter electrode

is a 3cm × 3cm platinum plate. The potential of -2.5V (vs. SSE) is applied to the copper substrate for electrodeposition. The electrodeposition time is 600 s. Nitrogen flow was bubbled into the solution during electrodeposition. The film obtained with solution A was washed with pure water, and the film obtained with solution B was washed with acetone.

The crystal structure of the film was determined using an X-ray diffractometer (Rigaku Co., Ltd. DMAX-2500) (target: Cu, tube voltage: 40 kV, tube current: 150 mA, incident angle θ: 1°, scanning step: 0.02°, FT time: 600 ms). Xe plasma FIB-SEM (PFIB-SEM) Thermo Fisher Scientific FEI Helios G4 PFIB CXe equipped with Ametek EDAX Octane Elite (70 mm2 SDD) and TOF-SIMS was used for surface and cross-sectional observation and compositional analysis of the film. An energy-dispersive X-ray spectrometer (EDS) and TOF-SIMS were used for elemental maps and component analysis of the surface and cross-section of the film. For TEM observation, a JEOL JEM-3000F (acceleration voltage: 297 kV) equipped with a Gatan post-column energy filter GIF-200 was used. The samples were processed into thin sections using the micro-pickup method using a Ga-FIB processing machine FB-2100 manufactured by Hitachi High-Technologies Corporation.

2.3 Results and Discussion

2.3.1 Surface Observation and XRD Diffraction

Figure 1 shows the SEM images of the surfaces of deposited films obtained from solution A (without $LiClO_4$) and solution B (with $LiClO_4$). Hereinafter, they will be referred to as Film A and Film B, respectively. Film A is dense and the surface is filled with precipitated particles. Since polishing scratches on the copper substrate remained, the thickness of the deposited film is thought to be thin. There were small cracks in the film, indicating that tensile stress had occurred in the film. On the other hand, the surface of film B is significantly different from film A, with coarse crystalline

particles embedded in the film. These crystalline particles are NaCl that cannot be washed away by acetone and are derived from the molecular sieves used in the dehydration process (see detailed description later). Since no polishing scratches are visible on the film, it can be assumed that the film is thick. Additionally, many coarse cracks occurred in the film, and some particles fell off, as shown by the red circles in the figure. Since Film B falls off the copper substrate when it comes into contact with water (the reason will be explained later), acetone was used instead of water to clean the remaining solution on the film surface. However, because the particles were embedded in the film, most of them seem to have remained.

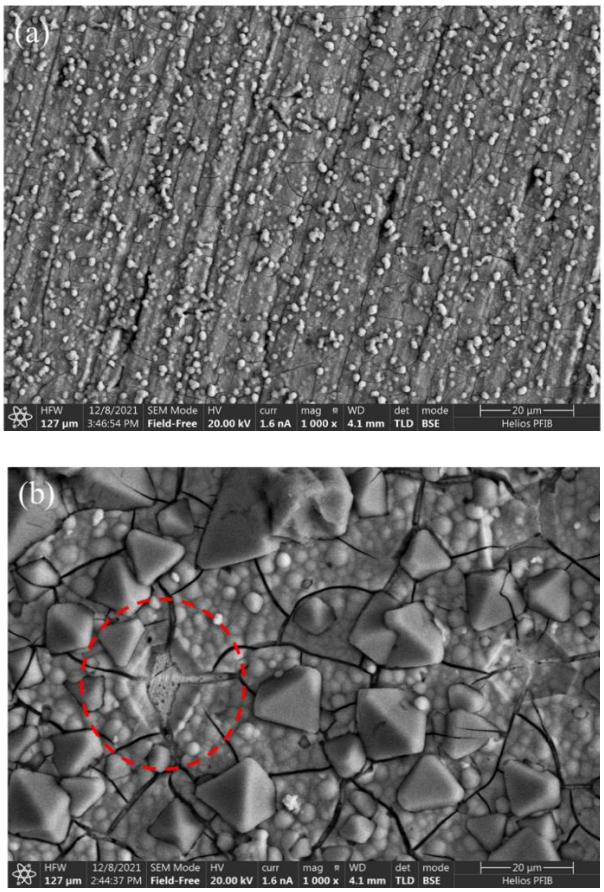

Fig.1 Plane-view SEM image of film A and B obtained in solutions without (a) and with $LiClO_4$ (b).

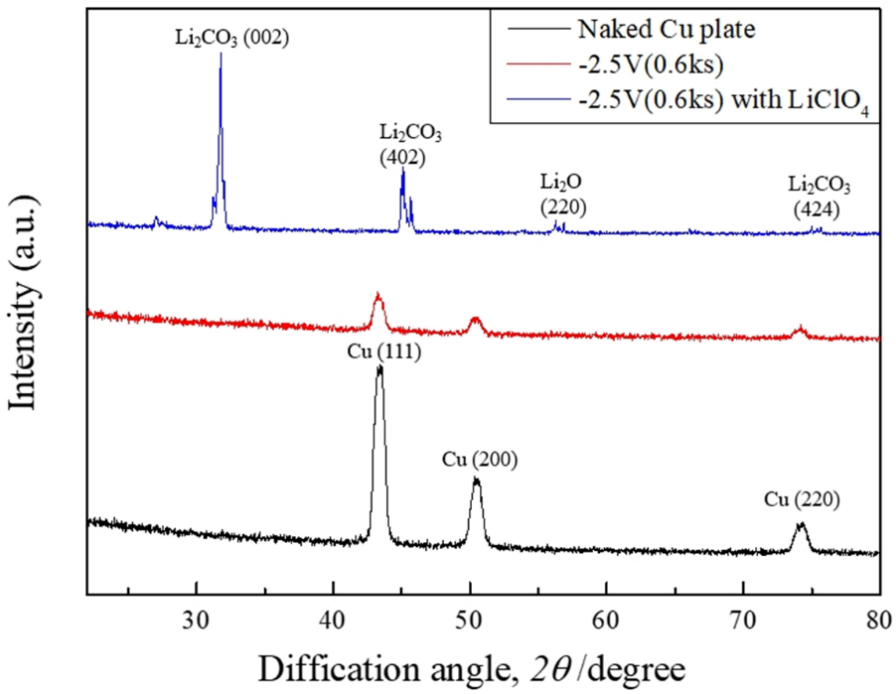

Fig. 2 Grazing-incidence X-ray diffraction patterns of the copper plate without film (a), with film A (b), and with film B (c).

Figure 2 shows the X-ray diffraction patterns of the electrodeposited specimen and the comparison copper plate. In film A, a diffraction peak from the copper substrate was detected, but in film B, no peak from the copper substrate was detected. Since no peaks other than copper appeared in film A, it can be seen that the crystal grains were either small or amorphous. On the other hand, in film B, there are no diffraction peaks from the copper substrate, but diffraction peaks from Li_2CO_3, Li_2O, and NaCl are observed. Note that the peak from NaCl is thought to originate from the coarse particles shown in Figure 1(b). However, since no metal-related peaks are observed, it is thought that film B is also composed of fine crystals or is amorphous.

2.3.2 Composition Analysis from Surface and Cross-Section

Figure 3 shows the EDS spectra and semi-quantitative analysis results obtained from a 130 μm × 100 μm area of the surface of film A (a), the surface of film B (b), and the back surface of film B peeled from the copper substrate (c). Large amounts of

carbon (C) and oxygen (O) were detected from all films, but no nitrogen (N) was detected. Since the quantitative nature of light elements such as C and O is low, both elements were excluded and the total concentration was normalized to 100%. In consideration of the detection limit, elements whose concentration was 1 at% or less are not listed. Sodium (Na) and chlorine (Cl) detected on the surface of film B are much higher than on the surface of film A. This is because NaCl particles remained that could not be removed by acetone washing. The Cu peak originates from the substrate, and because film A is thin, it was detected from both the substrate and the crack, and film B was detected through the crack. Since almost no copper was detected on the back side of film B, it can be said that there is no copper contained in the film. Regarding the Mn, Fe, Co, and Ni elements in the film, except that the Ni element content in film A is 3 to 5 times more than that of other elements, any film has a difference of about 2 to 3 times.

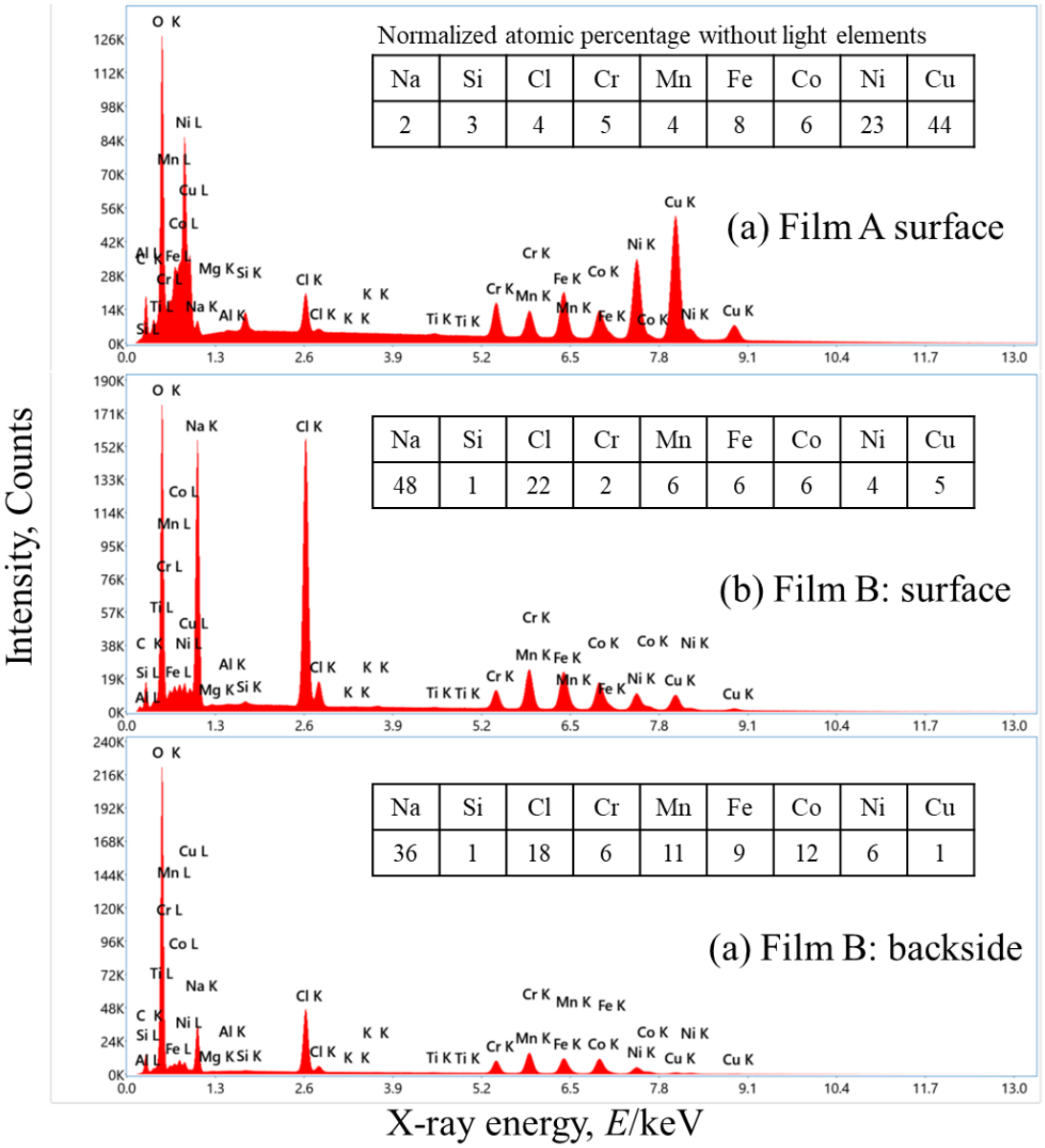

Fig.3 EDS spectrum of film A and film B, with semi-quantitative analyzed atomic percentage.

Figures 4 and 5 show SEM-EDS elemental maps of the surfaces of both films measured at an accelerating voltage of 20 kV. On the surface of film A (Figure 4), the distribution of Cr, Mn, Fe, Co, Ni, and C is almost uniform. However, some spherical particles and agglomeration of oxygen are detected around them (d). In addition, Cl and Na appeared at almost the exact location of the particles, suggesting that NaCl was attached to the surface. The respective positions do not necessarily correspond to the positions of all the spherical bodies in Figure 4(a), but this is probably because the penetration depth of the electron beam (approximately 1 μm) is much deeper than the

particle diameter. In film B (Figure 5), Cl and Na were detected in coarse particles, which correspond to NaCl, which appeared as the X-ray diffraction peak. The NaCl particles are thought to have precipitated from the Na in the molecular sieves and Cl in the chlorides that remained in the solution and may have been incorporated into the film while growing during the film formation process. In the film without NaCl particles, the distribution of Cr, Mn, Fe, Co, Ni, C, N, and O is uniform. Note that copper on the board was detected from the cracks in the film.

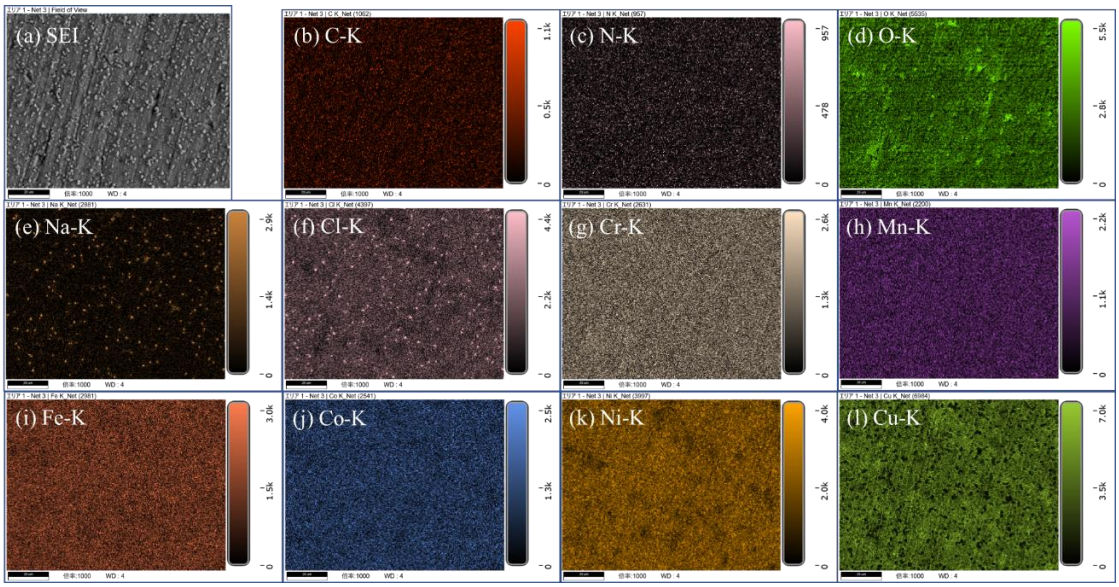

Fig.4 Plane-view SEM-EDS element maps (20kV) of film A.

As mentioned above, unlike Film A, Film B peels off when washed with water. Film B was formed by the addition of $LiClO_4$ so that lithium may be involved in the case. In the XRD analysis, as shown in Figure 2, diffraction peaks corresponding to Li_2CO_3 and Li_2O were detected, but it is unclear whether they exist only on the surface of film B or also inside the film. However, since the light element lithium cannot be detected using the EDS analysis method, the cross-section of the film was analyzed using the TOF-SIMS method, which can detect lithium.

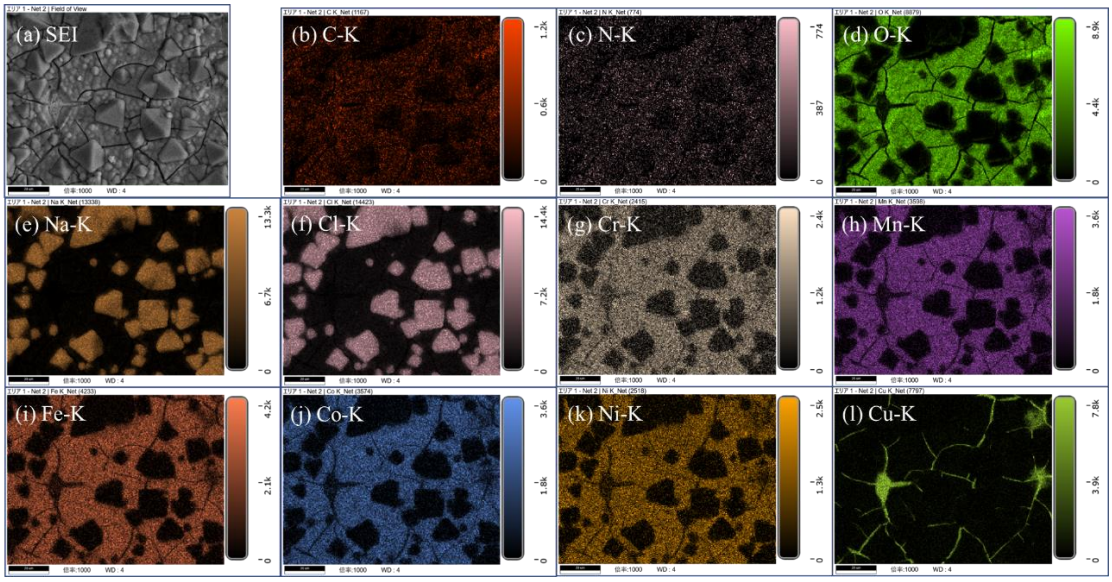

Fig.5 Plane-view SEM-EDS element maps (20kV) of film B.

Figure 6 shows the distribution of each element obtained by TOF-SIMS analysis of the cross-section of Film B. Figure 7 shows an SEM-EDS elemental map image of almost the same area. The sample was coated with a protective film of 98% Pt + 2% C and then processed in a cross-section, and vertical streaks from processing remained. Note that TOF-SIMS uses Xe ions from the PFIB device as primary ions, scans them in the same way as regular SIM image observation, and acquires the secondary ions emitted by the irradiation with a time-of-flight (TOF) analyzer. In addition, the irradiation current was set to 0.3 nA, lower than during processing, and elements (b) to (i) were measured as cations and elements (j) to (l) were measured as anions. However, SIMS results are not quantitative because they are significantly affected by the matrix effect of coexisting elements (a phenomenon in which coexisting elements change the secondary ion strength and reduce quantitative performance) [31] and unevenness. In addition, the SEM-EDS map was measured at a low accelerating voltage of 3 kV in order to prevent the penetration of electron beams and secondary excitation of X-rays and to ensure spatial resolution equivalent to TOF-SIMS. For this reason, it was not possible to obtain a chlorine (Cl) map.

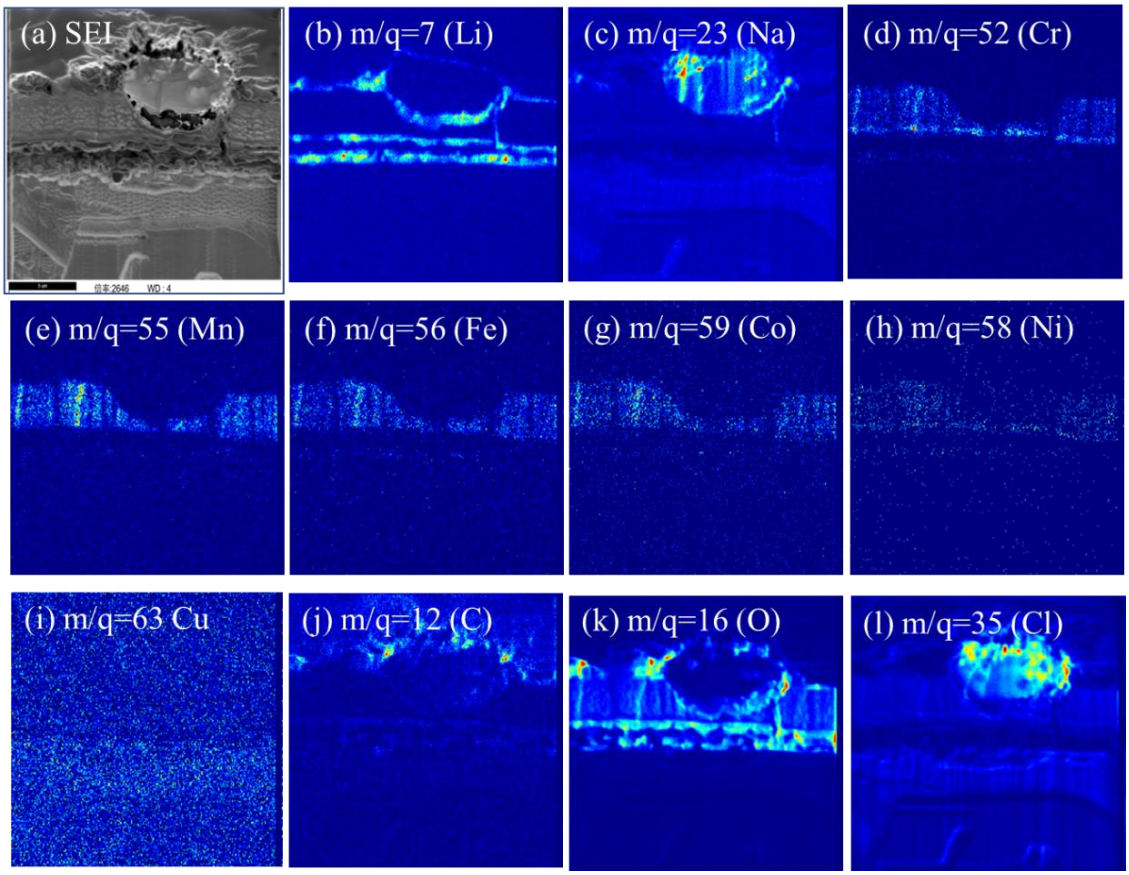

Fig.6 Cross-sectional TOF-SIMS intensity maps of film B.

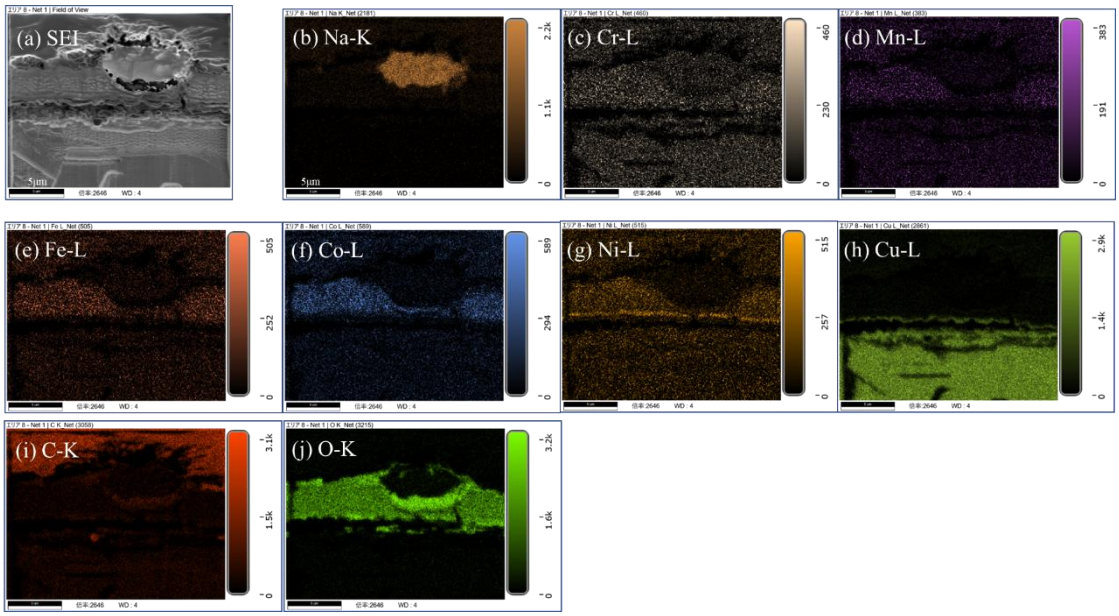

Fig.7 Cross-sectional SEM-EDS element maps (3kV) of film B.

From Figures 6(a) and 7(a), it can be seen that the coarse NaCl particles precipitated and grew during the electrodeposited film and could not be removed by the subsequent acetone cleaning. Li, O, and C were detected intermittently in the outer layer of the film. The carbon in the outer layer of the film shown in Figure 6 (j) is stronger than the protective layer above it (98% Pt + 2% C). Therefore, the outer layer of the film is thought to correspond to lithium oxide (Li_2O) or carbonate (Li_2CO_3) detected by X-ray diffraction. Note that although Li and O are detected below the NaCl particles, carbon is not detected, so it is thought that only Li_2O is formed. Cr, Mn, Fe, Co, and Ni in the middle layer of the film are almost uniform, but their strength is weaker than O. The reason for the low sensitivity of Cr, Mn, Fe, Co, and Ni in TOF-SIMS is presumed to be due to the matrix effect mentioned above. Furthermore, no significant amount of lithium was detected in the intermediate layer. Strong Li and O signals appear at the edge of the inner layer below the intermediate layer. Since there are few metal atoms and carbon in this region, it is thought that there are many lithium oxides in this layer. It is also possible that the lithium oxides and carbonates in the outer layer of the film formed when lithium in the deposited layer diffused out and reacted with air. On the other hand, the inner layer of lithium oxide is thought to have formed at the early stage of electrodeposition. Film B peels off from the copper substrate during water washing and remains as small pieces. This corresponds to the dissolution of lithium oxide at the interface.

In addition to the EDS and TOF-SIMS analysis described above, the surface of the film was etched by approximately 20 nm (vs. SiO_2) using Ar^+ ions and then analyzed using X-ray photoelectron spectroscopy (XPS). Figure 8 shows the spectra of Li 1s, C 1s, O 1s, Cr 2p, Mn 2p, Fe 2p, Co 2p, and Ni 2p detected in both films. Most Cr, Mn, and Fe on the surface of film A are in the oxidized state, and most Co and Ni are in the metallic state. In addition, C 1s and O 1s indicate a bonding state between carbon, oxygen, and metal. Many lithium oxides or carbonates are detected on the surface of film B, but the amounts of Cr, Mn, Fe, Co, and Ni is extremely low. This corresponds to the analysis results for the outer layer of the film (Figure 6).

For Cr, Mn, Fe, Co, and Ni, the mixing entropy ΔS_{mix} of film A and film B is

calculated to be 1.37R and 1.55R (R: gas constant), respectively. In general, alloys with $\Delta S_{mix} \geqq 1.5R$ are considered as high-entropy alloys. This means film A is a medium-entropy alloy, and film B is a high-entropy alloy. On the other hand, both films contain large amounts of oxygen and carbon. Although the bonding states of various elements in the intermediate layer of film B are unknown, each metal element in film A has a complex chemical bonding state. In this study, such a film is referred to as a "CrMnFeCoNi-containing film" or an "oxygen-containing CrMnFeCoNi film".

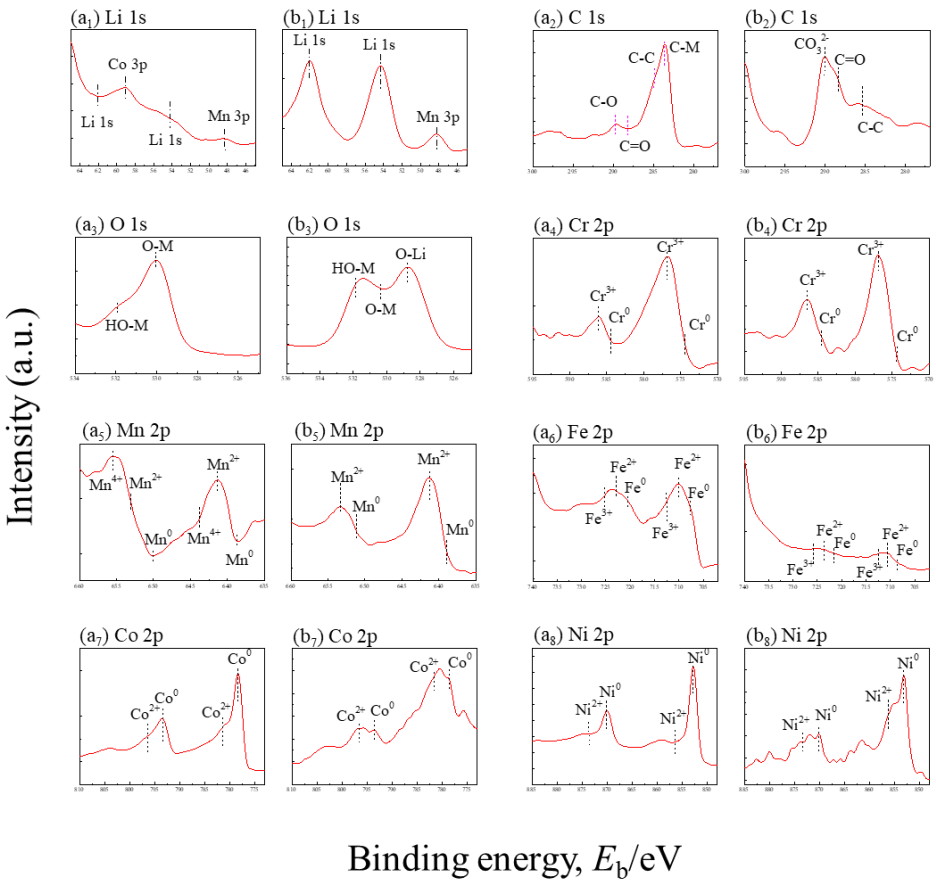

Fig. 8 XPS spectra of Li 1s, C 1 s, O 1 s, Cr 2 p, Mn 2 p, Fe 2 p, Co 2 p, and Ni 2 p from films A and B. The analysis was conducted after Ar^+ sputter etching for 6.0 ks.

2.3.3 Cross-Sectional Observation by TEM

Figures 9 to 11 show the results of TEM observation of cross-sectional thin sections

of both films A and B processed using the Ga-FIB micro pickup method (low magnification bright field image, high-resolution image, and selected area electron diffraction pattern). All high-resolution images are zero-loss images obtained by inserting a 10 eV slit in a post-column energy filter to remove inelastically scattered electrons.

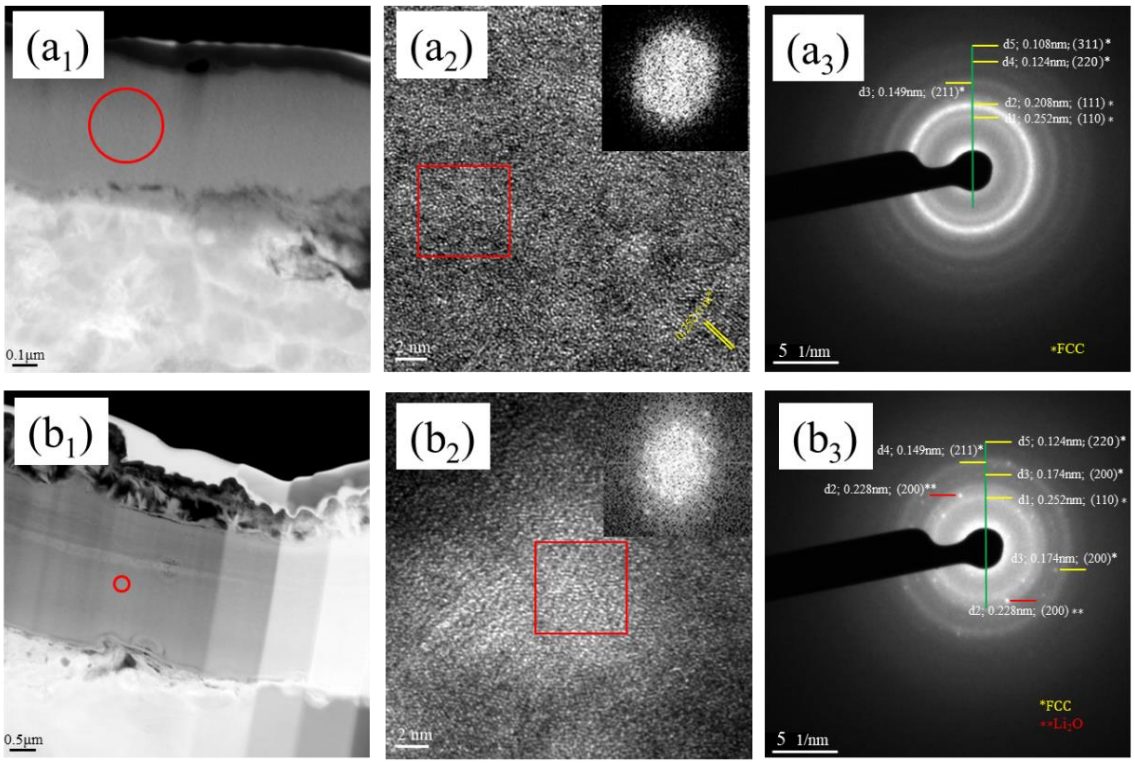

Fig.9 Cross-sectional TEM images. Bright-field image (low magnification: (a_1, b_1)), High-resolution electron microscopy image (HREM, Zero loss image ΔE = 10eV, FFT of red square: (a_2, b_2)), and selected area electron diffraction (SAD) pattern (a_3, b_3) of film A (a_1~a_3) and film B (b_1~b_3). The selected area aperture was placed on the red circle in a1 and b1.

In film A shown in Figure 9(a), the low magnification bright field image (a1) shows that the film is dense, approximately 0.5 μm thick, and adheres closely to the copper substrate. Although no clear long-range ordered structure is seen in the high-resolution image (a_2), spots appear when fast Fourier transform (FFT) is performed locally, and diffraction rings are also seen in the selected area diffraction image (a_3). This indicates that film A contains nanocrystal aggregates that were not detected by

X-ray diffraction in Figure 2. The crystal plane spacing of the diffraction rings (d_1 to d_5) corresponds to a CrMnFeCoNi alloy [32] with a face-centered cubic structure (FCC). Therefore, it can be seen that film A contains CrMnFeCoNi nanocrystals in an amorphous structure with low crystallinity.

On the other hand, according to Figure 9(b), the thickness of film B is thicker than film A, approximately 3.6 μm. When FFT locally analyzes the high-resolution image (b2) of the intermediate layer, spots appear in this layer as well, and it can be determined that there are nanocrystals. Additionally, polycrystalline diffraction rings and numerous diffraction spots appeared in the electron diffraction pattern (b_3). The diffraction rings (d_1, d_3 to d_5) correspond to CrMnFeCoNi nanocrystals as in Fig. 9 (a_3), and the diffraction spot (d_2) can be attributed to Li_2O. This result corresponds to the XRD diffraction (Figure 2), and it is thought that CrMnFeCoNi nanocrystals and Li_2O partially exist in the amorphous structure. Figure 10 shows the results of detailed observation and analysis of the outer layer. Large crystals and nanodentrites can be seen next to them. A large number of CrMnFeCoNi alloy, Li_2O, and Li_2CO_3 nanocrystals were observed in the high-resolution image (c). In addition, diffraction spots corresponding to the nanocrystals in (c) were observed in the electron diffraction image (d). As can be seen, the structure of the outer layer is significantly different from that of the middle layer shown in Figure 9(b).

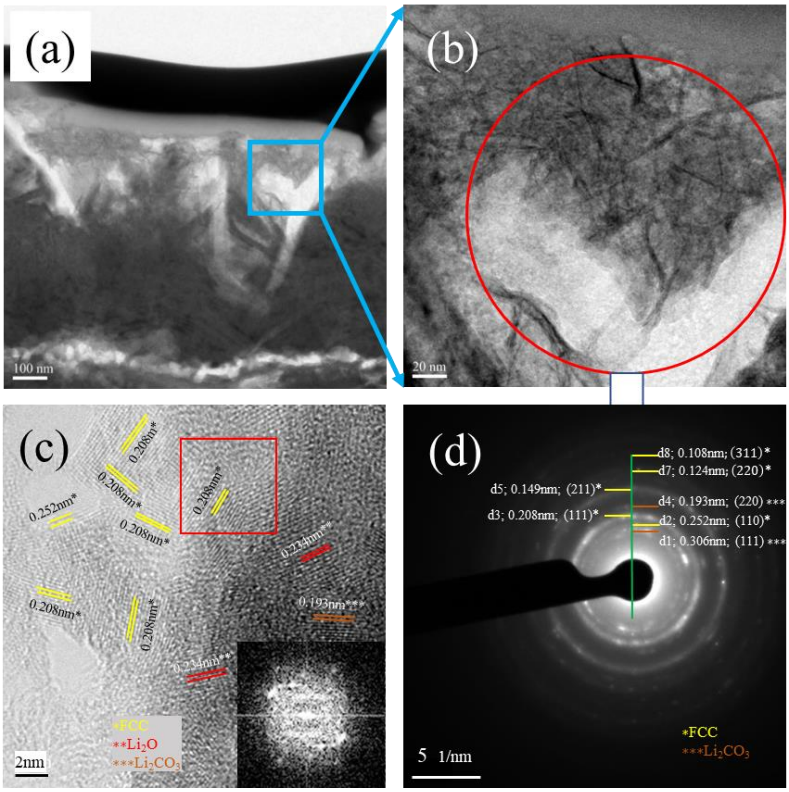

Fig.10 Cross-sectional TEM images. Bright-field image (a, b) of the outer side of film B, High-resolution electron microscopy image (HREM, Zero loss image ΔE = 10eV, FFT of red square (c)), and selected area electron diffraction (SAD) pattern (d). The selected area aperture was placed on the red circle in (b).

Figure 11 shows bright-field images before and after the intermediate layer of film B was irradiated with an electron beam. Before irradiation, a streak-like structure was visible, but after irradiation, the appearance changed significantly, indicating that it had transformed into nanospheres. This instability caused by electron beam irradiation is thought to be caused by the decomposition of a small amount of lithium oxide contained in the film.

From the above observations, it was found that under the experimental conditions used in this study, the addition of $LiClO_4$ significantly increased the film growth rate by about 7 times. However, it was found that the formed film was not only divided into three layers but also contained coarse NaCl, which caused peeling when immersed in water. However, the intermediate layer of film B is considered to be a uniform high-entropy alloy layer.

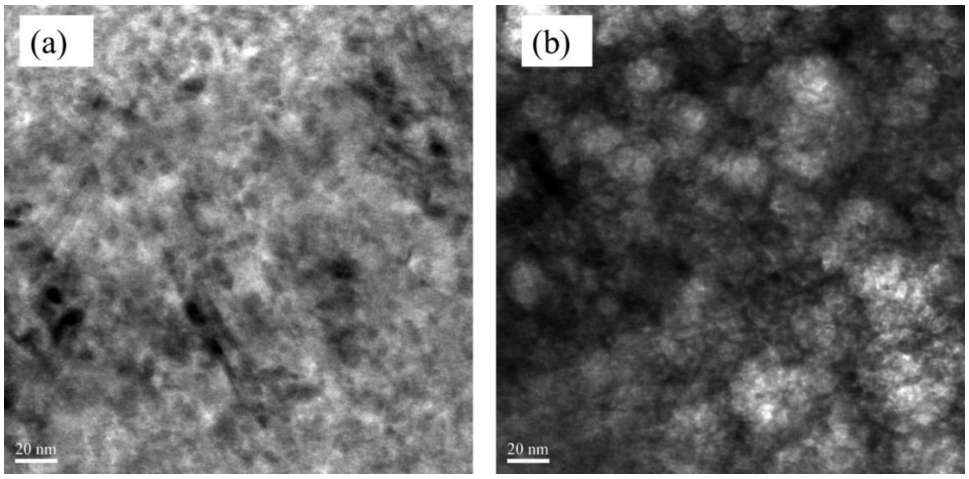

Fig.11 Bright field image of film B before (a) and after (b) electron irradiation.

2.3.4 Precipitation Behavior in Electrodeposition

In electrodeposition, each metal ion generally has its unique deposition potential, and if the applied potential is nobler than the deposition potential, no deposition occurs. The less noble the applied potential, the faster the deposition rate. [16, 26)] In a preliminary experiment, when a potential of 0 to -3.0 V (vs. SSE) was applied to the solvent, no reaction current was observed, confirming that the DMF-CH_3CN solver itself was stable. In this study, Cr, Mn, Fe, Co, and Ni were simultaneously incorporated as alloys into thin films in both solutions at an applied potential of -2.5 V (vs. SSE). Therefore, each metal ion did not precipitate alone, but a eutectoid reaction occurred. Such eutectoid reaction is thought to be related to the formation of a complex ($[M(DMF)_6]^{2+}$) between the metal ion and the solvent (DMF-CH_3CN). [16, 33, 34)] The electrodeposition behavior in the solutions used in this article is described below.

Figure 12 shows the relationship between time and deposition current for solution A without adding the supporting electrolyte $LiClO_4$ and solution B with $LiClO_4$ added. In the case of solution A, the deposition current remained almost constant until the end, except for a decrease in current during the first 20 s. The deposited film contains a large amount of oxygen and a large amount of carbon. Before and during

electrodeposition, nitrogen was bubbled into the solution to remove oxygen, so a small amount of dissolved oxygen should be present. In contrast, a large amount of oxygen in the film is thought to originate from DMF (C_3H_7NO). Similarly, the carbon in the film separated from DMF and CH_3CN. Therefore, DMF and CH_3CN appear to be involved in the eutectoid reactions of Cr, Mn, Fe, Co, and Ni.

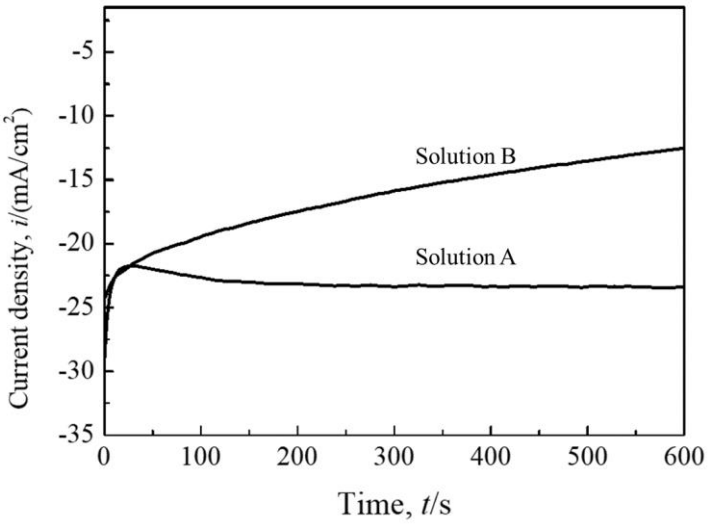

Fig.12 Potentiostatic chronocurrent curves on a Cu plate at applied potentials of -2.5V (vs. SSE) in solutions A and B.

On the other hand, in the case of solution B containing the supporting electrolyte $LiClO_4$, the electrodeposition absolute value of current continued to decrease from the start of electrodeposition to the end of electrodeposition. As in the case of solution A without $LiClO_4$, during electrodeposition, Cr^{3+}, Mn^{2+}, Fe^{2+}, Co^{2+}, and Ni^{2+} undergo a eutectoid reaction with the involvement of DMF and CH_3CN. In addition, it is assumed that at the early stage of electrodeposition, lithium ions (Li^+) with a small ionic radius and low charge were involved in building an electric double layer, resulting in the formation of Li_2O. After the large and rapid consumption of Li^+ by the formation of the inner layer, Cr^{3+}, Mn^{2+}, Fe^{2+}, Co^{2+}, and Ni^{2+} appear to undergo eutectoid reactions on the copper substrate and become the intermediate layer of the film while trapping oxygen and carbon. In addition, it is thought that the Na in the

molecular sieves remaining in the solution reacted with the Cl in the solution, and the precipitated NaCl was incorporated into the film while growing as coarse crystals. After the electrodeposition was completed, lithium diffused from the intermediate layer to the surface, and Li^+ adsorbed on the surface was likely to combine with oxygen and carbon dioxide in the air to form oxides or carbonates. As described above, in film B, lithium oxide and NaCl with high electrical resistance were formed, so the current gradually decreased and the film growth rate increased, but the film became multilayered.

Lithium-containing CrMnFeCoNi alloy film B also contains oxygen and carbon, is unstable in water, and is damaged by electron irradiation. Film B has a three-layer structure, is not uniform, and is highly reactive with water. However, by adjusting the amount of $LiClO_4$ added and the applied voltage, it is possible to form a CrMnFeCoNi alloy film with the same composition as the intermediate layer at high speed. On the other hand, Film A, which does not contain lithium compounds, has stability in water, durability against electron irradiation and excellent mechanical properties, and can be expected to be used as an oxygen generation catalyst. [35] Plans include a more detailed study of the composition and structure of the film and, in particular, investigate functionality related to metal oxides and carbides.

2.4 Conclusion

Thin films containing CrMnFeCoNi were prepared by electrodeposition on copper substrates using an organic solvent (DMF-CH_3CN) (potential -2.5 V (vs. SSE), 600 s). SEM, XRD, EDS, TOF-SIMS and TEM were used to study the surface morphology, composition, crystal structure, etc. of film A formed without adding supporting electrolyte $LiClO_4$ in the solvent and film B formed with adding supporting electrolyte. The results obtained are as follows.

(1) By using an organic solvent, a film containing CrMnFeCoNi with a high mixing entropy can be obtained regardless of the addition of a supporting electrolyte. Both

films contain large amounts of oxygen and carbon.

(2) The thickness of film A is approximately 0.5 μm, and Cr, Mn, Fe, Co, Ni, C, and O are uniformly distributed in the film. This film has an amorphous structure containing nanocrystals.

(3) Film B is approximately 3.6 μm thick. The addition of supporting electrolyte inhibits the formation of a uniform film, and Film B easily peels off in water. $LiClO_4$ does not play an influential role in obtaining a stable film.

References

1) J.W. Yeh, S.K. Chen, J.Y. Gan, S.J. Lin, T.S. Chin, T.T. Shun, C.H. Tsau, S.Y. Chang; Metall. Mater. Trans. A; 35, 2533-2536, 2004.

2) W. Zhang, P.K. Liaw, Y. Zhang; Science China Materials; 61, 2-88, 2018.

3) Y. Wu, F. Zhang, X. Yuan, H. Huang, X. Wen, Y. Wang, M. Zhang, H. Wu, X. Liu, H. Wang, S. Jiang, Z. Lu; Journal of Materials Science & Technology; 62, 214-220, 2021.

4) X.H. Du, W.P. Li, H.T. Chang, T. Yang, G.S. Duan, B.L. Wu, J.C. Huang, F.R. Chen, C.T. Liu, W.S. Chuang, Y. Lu, M.L. Sui, E.W. Huang; Nature Communications; 11, 2390, 2020.

5) X. Lu, J. Zhao, C. Yu, Z. Li, Q. Kan, G. Kang, X. Zhang; J. Mech. Phys. Solids; 142, 103971, 2020.

6) L.L. Xiao, Z.Q. Zheng, S.W. Guo, P. Huang, F. Wang; Materials & Design; 194, 108895, 2020.

7) S. Yoshida, T. Ikeuchi, T. Bhattacharjee, Y. Bai, A. Shibata, N. Tsuji; Journal of the Japan Society of Powder and Powder Metallurgy; 67, 113-120, 2020.

8) N. Tsuji, N. Park, X. Li, R.R. Eleti, S. Yoshida, T. Bhattacharjee, Y. Bai, P.P. Bhattacharjee, S. Kurokawa; Materia Japan; 57, 317-322, 2018.

9) N.L. Okamoto, K. Yuge, H. Inui; Materia Japan; 57, 312-316, 2018.

10) X.W. Qiu, M.J. Wu, C.G. Liu, Y.P. Zhang, C.X. Huang; J. Alloys Compd.; 708,

353-357, 2017.

11) Y. Qiu, S. Thomas, M.A. Gibson, H.L. Fraser, N. Birbilis; npj Materials Degradation; 1, 15, 2017.

12) X. Shang, Z. Wang, F. He, J. Wang, J. Li, J. Yu; Science China Technological Sciences; 61, 189-196, 2017.

13) Q. Ye, K. Feng, Z. Li, F. Lu, R. Li, J. Huang, Y. Wu; Appl. Surf. Sci.; 396, 1420-1426, 2017.

14) C.Z. Yao, P. Zhang, M. Liu, G.R. Li, J.Q. Ye, P. Liu, Y.X. Tong; Electrochim. Acta; 53, 8359-8365, 2008.

15) C.Z. Yao, P. Zhang, Y.X. Tong, D.X. Xia, H.X. Ma; Chem. Res. Chinese Univerisities; 26, 640-644, 2010.

16) C. Yao, H. Ma, Y. Tong; Chinese Journal of Applied Chemistry; 28, 1189-1194, 2011.

17) M.H. Tsai, J.W. Yeh; Materials Research Letters; 2, 107-123, 2014.

18) M. Vaidya, A. Karati, A. Marshal, K.G. Pradeep, B.S. Murty; J. Alloys Compd.; 770, 1004-1015, 2019.

19) K. Fujita, H. Fujiwara, S. Kikuchi; Journal of the Society of Materials Science, Japan; 70, 648-655, 2021.

20) X.H. Yan, J.S. Li, W.R. Zhang, Y. Zhang; Mater. Chem. Phys.; 210, 12-19, 2018.

21) A. Sharma; Coatings; 11, 372, 2021.

22) W. Li, P. Liu, P.K. Liaw; Materials Research Letters; 6, 199-229, 2018.

23) X. Li, Z. Zheng, D. Dou, J. Li; Materials Research; 19, 802-806, 2016.

24) L. Gao, W. Liao, H. Zhang, J. Surjadi, D. Sun, Y. Lu; Coatings; 7, 156, 2017.

25) J. Wang, S. Wu, S. Fu, S. Liu, M. Yan, Q. Lai, S. Lan, H. Hahn, T. Feng; Scripta Mater.; 187, 335-339, 2020.

26) T. Morikawa; Journal of The Surface Finishing Society of Japan; 72, 576-585, 2021.

27) H. Li, H. Sun, C. Wang, B. Wei, C. Yao, Y. Tong, H. Ma; J. Alloys Compd.; 598, 161-165, 2014.

28) M. Zheng, Y. Li, J. Hu, Y. Zhao, L. Yu; MSAIJ; 11, 344-348, 2014.

29) V. Soare, M. Burada, I. Constantin, D. Mitrică, V. Bădiliţă, A. Caragea, M. Târcolea; Appl. Surf. Sci.; 358, 533-539, 2015.

30) A. Aliyu, C. Srivastava; Thin Solid Films; 686, 137434, 2019.

31) S. Aoyagi; Vacuum and Surface Science; 62, 211-216, 2019.

32) S.H. Joo, H. Kato, M.J. Jang, J. Moon, E.B. Kim, S.J. Hong, H.S. Kim; J. Alloys Compd.; 698, 591-604, 2017.

33) H. Sakiyama, M. Ito, R. Mitsuhashi, M. Mikuriya; Journal of Computer Chemistry, Japan; 15, 49-50, 2016.

34) M. Ito, R. Mitsuhashi, M. Mikuriya, H. Sakiyama; X-Ray Structure Analysis Onlin; 32, 21-22, 2016.

35) T. Xiao, R. Wang, E. Tanabe, Y. Satoh, M. Bazzaoui, Y. Ling, Z. Lu; Coatings; 12, 1804, 2022.

Chapter 3 Fabrication and Characterization of Oxygen-Containing CrMnFeCoNi Films Electrodeposited in DMF-CH_3CN Solution with and without Supporting Electrolyte $LiClO_4$

3.1 Introduction

In Chapter 2, electrodeposition was performed at -2.5 V (vs. SSE) in the organic solvent of DMF-CH_3CN containing metal ions of Cr^{3+}, Mn^{2+}, Fe^{2+}, Co^{2+}, and Ni^{2+}. Amorphous films of CrMnFeCoNi containing large amounts of oxygen and carbon were obtained. They are different from the literature on pure high entropy alloy of CrMnFeCoNi, being novel as an oxygen-containing HEA film. Some carbon was also included. In preparation for such oxygen-containing HEA film, the usually applied supporting electrolyte of $LiClO_4$ does not play an influential role in obtaining a stable film. On the other hand, in the solution in the absence of $LiClO_4$, a compact and stable film was successfully synthesized.

On the other hand, the different applied potentials can generally change the composition of films. This depends on the reduction behavior of each metal ion. In this chapter, the potential was expanded, and the reduction behavior of each metal ion was investigated. Furthermore, the oxygen evolution reaction activity was measured.

3.2 Experiment

The size of the electrodeposited substrate and the pretreatment method are the same

as in the previous chapter.

Electrodeposition was performed in a glass breaker containing organic solvent-based bath solutions at 313 ± 1 K. An electrochemical workstation (CS350, Wuhan Corrtest Inst. Co.) was used to apply a constant potential: a saturated silver/silver chloride electrode (SSE, 0.1976 V vs. reversible hydrogen electrode (RHE)) was used as the reference- and a platinum plate as the counter-electrode. The difference here from Chapter 2 is that, together with our preliminary research, the discussion is carried out on the basis of three solutions. In the bath solution, designated metal chlorides: $CrCl_3 \cdot 6H_2O$, $MnCl_2$, $FeCl_2 \cdot 4H_2O$, $CoCl_2$, and $NiCl_2 \cdot 6H_2O$, were added to the DMF-CH_3CN (4:1 by volume) solvent. Unlike other reports, [1-4] I confirmed the insolubility of anhydrous chlorides $CrCl_3$ and $NiCl_2$ in the solvent. Therefore, chemicals $CrCl_3 \cdot 6H_2O$ and $NiCl_2 \cdot 6H_2O$ were used. $FeCl_2 \cdot 4H_2O$ was chosen due to availability. As shown in Table 1, three solutions, A, B, and C, were prepared for the deposition, with 0.1 M $LiClO_4$ as the supporting electrolyte contained in only solution A. The concentrations of chlorides were adjusted in solutions B and C to enhance conductivity and obtain different film compositions. After dissolving the metal chlorides or $LiClO_4$ in the solvent, the solutions were dehydrated with molecular sieves (4A 1/8, Fujifilm Wako Pure Chemical Co.) for 43.2 ks then deaerated by nitrogen gas (purity: 99.999%) for 3.6 ks before and during the deposition, with the molecular sieves remaining at the bottom of the solution.

Table 1 Electrolytes for electrodeposition. Metal chlorides with various concentrations were contained in an organic solvent of DMF and CH_3CN (4:1 by volume).

Electrolyte	$CrCl_3$ (M)	$MnCl_2$ (M)	$FeCl_2$ (M)	$CoCl_2$ (M)	$NiCl_2$ (M)	$LiClO_4$ (M)	Total cations (M)
A	0.01	0.01	0.01	0.01	0.01	0.1	0.15
B	0.03	0.03	0.03	0.03	0.03	-	0.15
C	0.06	0.1	0.04	0.06	0.02	-	0.28

Potentials for triggering the reduction reaction of the respective metal ions on a Cu substrate with a diameter of 1.0 mm were investigated in organic solvent containing

chlorides of different metals by measuring the cyclic voltammetry (CV) curves at the scanning rate 100 mV/s. Based on these measurements, the deposition in electrolytes A, B, and C on the Cu plate was performed at -2.0 V, -2.5 V, and -3.0 V (vs. SSE) for 0.6 and 1.8 ks. Note that substrates were rinsed in 5 % hydrochloric acid, distilled water, and acetone before CV measurement or electrodeposition.

The tests of SEM, SEM-EDS, XRD, FIB, FE-STEM and TOF-SIMS are the same as in Chapter 2.

X-ray photoelectron spectroscopy (XPS; AXIS ULTRA, Shimadzu Co.) was used to analyze chemical binding among film elements (analysis area: 2 mm x 1 mm) in a vacuum chamber under air pressure < 4 x 10^{-5} Pa. The X-ray was Mg Kα excited 15 kV and 10 mA. The pass energy was set as 40 eV. Before XPS analysis, the specimen surface was sputter-etched for 6.0 ks by accelerated argon ions (Ar^{+}) to eliminate contaminants and any oxide layer. A mixed Gauss-Lorentz function as 0.7:0.3 was used to split element peaks according to the binding energy of each chemical state. Relative average atomic concentrations were calculated using atomic sensitive factors (ASF).

Film hardness was measured by nanoindentation (DUH-201, Shimadzu Co.) to a maximum load of 40 nN. OER electrocatalytic property was evaluated in an aerated 1.0 M KOH aqueous solution at 303 ± 1 K by measuring linear sweep voltammetry (LSV) at a scanning rate of 5 mV/s. The potential was converted versus RHE, $E_{RHE} = E_{Ag/AgCl} + 0.060*pH + 0.1976$ (V), and the Tafel slope was obtained from the LSV curve in the kinetically controlled region.

3.3 Results and Discussion

3.3.1 Cyclic Voltammetry and Chronocurrent Curves

Fig. 1 (a) shows the CV curves obtained on the Cu disk (1.0 mm dia.) in DMF-CH_3CN with and without 0.1 M $LiClO_4$. In the absence of $LiClO_4$ (black line),

reaction peaks are not observed, regardless of dehydration by molecular sieves or not, demonstrating high stability of DMF-CH_3CN solvent in the potential scope of -3.0 ~ 0.0V (vs. SSE). In the presence of $LiClO_4$ in solution without dehydration (red line), a small peak at -0.69V and two wide peaks were observed near -1.92V and -2.76V (vs. SSE). After dehydration (blue line), the peak at -1.92V degenerated into two smaller ones at -1.66V and -2.11V, while those at -0.69V and -2.76V became much weaker.

In preliminary XPS analysis, lithium was not detected in the copper surface after applying a potential of -2.5 V for 0.6ks in the 0.1 M $LiClO_4$ -containing DMF-CH_3CN solution without the target metal ions. In contrast, a peak of Li 1s was observed under the potential of -3.0V. Therefore, the peak at -2.76V was considered to correspond to the reduction reaction of $Li^+ + e^- \rightarrow Li^0$, which is much nobler than that equilibrium value of -3.24V vs. SSE (0.1 M $LiCO_4$ solution at 313K). A more negative reduction potential of Li^+ was reported in an aqueous solution due to high hydration enthalpy [7]. Therefore, the weak hydration of Li^+ in the current organic solution might have promoted the above reduction. The peaks at -0.69 V and -2.11 V might correspond to the two-step oxygen reduction of $O_2 \rightarrow O_2^-$ and $O_2^- \rightarrow O_2^{2-}$ [8], whereas the peak at -1.66V might correspond to the reduction of dissolved water [9]. Water comes from $LiClO_4$ without dehydration, while oxygen originates from adsorbed air in the porous molecular sieves.

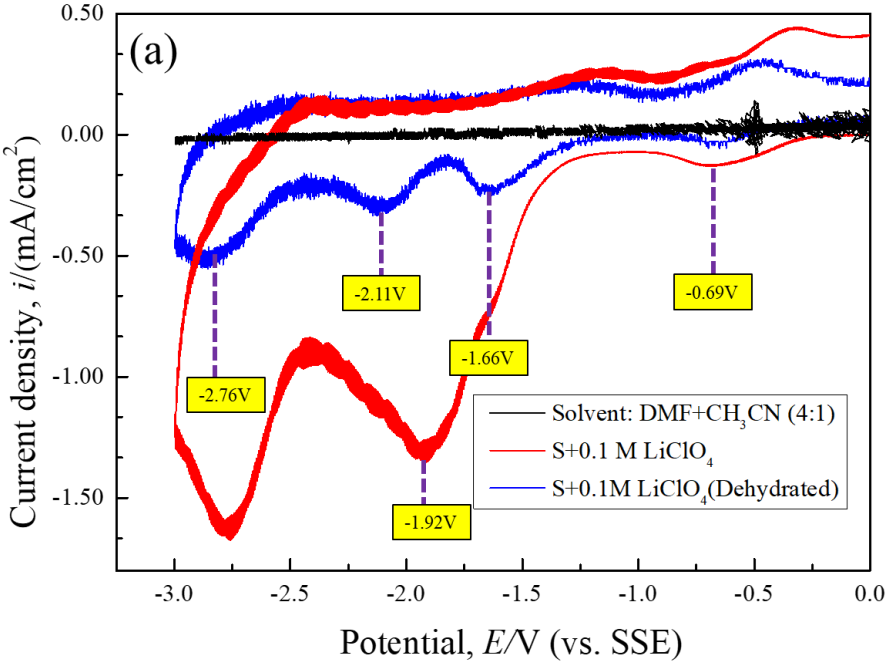
(a)
0.50
0.00
-0.50
-1.00
-1.50
Current density, i/(mA/cm2)
-3.0
-2.5
-2.0
-1.5
-1.0
-0.5
0.0
Potential, E/V (vs. SSE)
-2.76V
-2.11V
-1.92V
-1.66V
-0.69V
Solvent: DMF+CH3CN (4:1)
S+0.1 M LiClO4
S+0.1M LiClO4(Dehydrated)

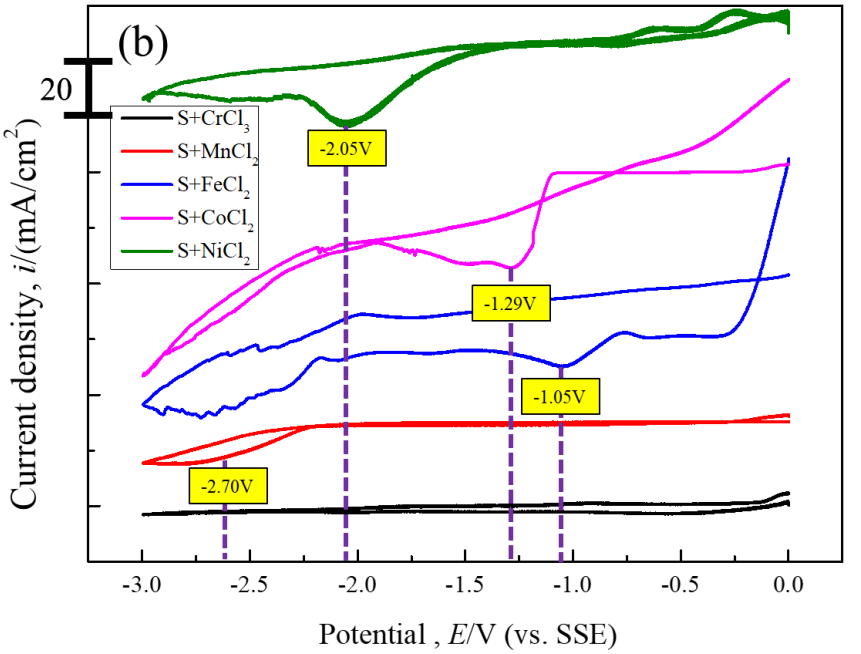
(b)
20
Current density, i/(mA/cm2)
S+CrCl3
S+MnCl2
S+FeCl2
S+CoCl2
S+NiCl2
-2.05V
-1.29V
-1.05V
-2.70V
-3.0
-2.5
-2.0
-1.5
-1.0
-0.5
0.0
Potential , E/V (vs. SSE)

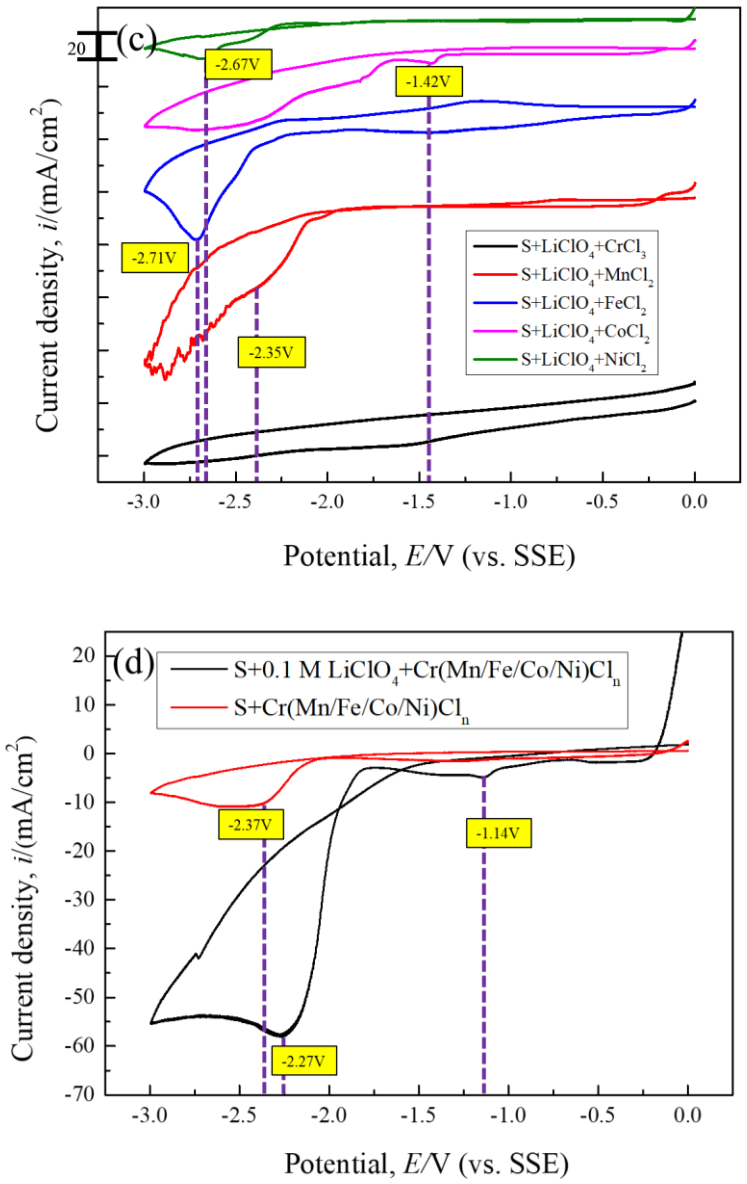

Fig. 1 Cyclic voltammetry curves obtained on a Cu disk (Φ: 1 mm), obtained in DMF-CH_3CN (4:1 by volume) solution at a sweep rate of 100mV/s.

(a) without and with containing 0.1M $LiClO_4$,

(b) Containing isolated 0.01M $FeCl_2$, $CoCl_2$ and 0.02M $CrCl_3$, $MnCl_2$, $NiCl_2$ without 0.1M $LiClO_4$,

(c) Containing isolated 0.01M $FeCl_2$, $CoCl_2$ and 0.02 M $CrCl_3$, $MnCl_2$, $NiCl_2$ with 0.1M $LiClO_4$,

(d) Containing 0.01M $CrCl_3$, 0.01M $MnCl_2$, 0.01M $FeCl_2$, 0.01M $CoCl_2$, and 0.01M $NiCl_2$ with and without 0.1M $LiClO_4$.

Fig. 1 (b) shows the CV curves in solutions containing isolated chloride: $FeCl_2$, $CoCl_2$ at 0.01M or $CrCl_3$, $MnCl_2$, $NiCl_2$ at 0.0_2 M. $LiClO_4$ was absent from all solutions. Dehydration and deaeration were applied before measurement. No reaction peak was detected in the CrCl3 solution, indicating the difficulty of reduction of Cr^{3+}. In contrast, reduction peaks were observed at -2.70 V for $MnCl_2$, -1.05 V for $FeCl_2$, -1.29 V for $CoCl_2$, and -2.05 V for $NiCl_2$, respectively. The current peaks in Fig. 1 (b) are larger than those in Fig. 1 (a). According to XPS analysis of isolated films obtained at -3.0 V from the above solutions, chromium showed a fully oxidized state (Cr^{3+}), whereas manganese, iron, cobalt, and nickel, respectively appeared at their elemental and oxidized states. Therefore, except for $CrCl_3$, the above four reaction peaks should correspond to the reduction potentials of the particular metal ions.

Fig. 1 (c) shows the CV curves in 0.1M $LiClO_4$-containing solutions with isolated chloride: $FeCl_2$, $CoCl_2$ at 0.01M or $CrCl_3$, $MnCl_2$, $NiCl_2$ at 0.02M, after dehydration and deaeration. As in Fig. 1 (b), reaction peaks are not seen in the $CrCl_3$ solution, while the current density in the $MnCl_2$ solution became larger after -2.5V. The potential peaks were obtained at -2.35V for $MnCl_2$, -2.71V for $FeCl_2$, -1.42V for $CoCl_2$, and -2.67V for $NiCl_2$. The potentials for $FeCl_2$ and $NiCl_2$ became negative compared to in Fig. 1 (b). These potentials differ from those reported by Yao et al. [1-4] and Soare et al. [6], perhaps due to our use of hydrous chemicals. The reason is unclear, but $LiClO_4$ surely affected the reduction potential of each target metal ion, especially since the current density after -2.5V became large.

Fig. 1 (d) shows the CV curves obtained in the solution of 0.01M $CrCl_3$ + 0.01M $MnCl_2$ + 0.01M $FeCl_2$ + 0.01M $CoCl_2$ + 0.01M $NiCl_2$ with and without 0.1M $LiClO_4$. Dehydration and deaeration were applied before measurement. The reduction current at -1.14V was relatively larger than without $LiClO_4$. In addition, the large currents between -2.0V and -3.0V might be related the to co-deposition of multi-metal ions. The reduction of Li^+ might also be involved in the case of solutions containing $LiClO_4$.

Based on these CV measurements, potentials -2.0V, -2.5V, and -3.0V (vs. SSE) were chosen to conduct electrodeposition. Fig.2 (a) shows the chronocurrent in solution A: 0.01M $CrCl_3$ + 0.01M $MnCl_2$ + 0.01M $FeCl_2$ + 0.01M $CoCl_2$ + 0.01M

$NiCl_2$ with 0.1M $LiClO_4$. The higher the applied negative-potential; the higher the resultant negative-current. Current continuously and largely decreased with deposition time, indicating instability of the electric double layer. A longer period was needed to reach a stable state at -3.0V, indicating a continuous accumulation of lithium ions at the electric double layer. Fig. 2 (b) shows the chronocurrent in solution C: 0.06M $CrCl_3$ + 0.1M $MnCl_2$ + 0.04M $FeCl_2$ + 0.06M $CoCl_2$ + 0.02M $NiCl_2$ in DMF-CH_3CN without $LiClO_4$. Almost a similar curve was obtained in solution B. The current sharply decreased after applying a designated potential and reached a stable value: higher negative-current under higher negative-potential. The rapid reduction of current in the initial 50 s should be related to the rapid formation of a stable electric double layer containing various metal ions. Some metal ions migrated to the Cu surface, and deposition occurred.

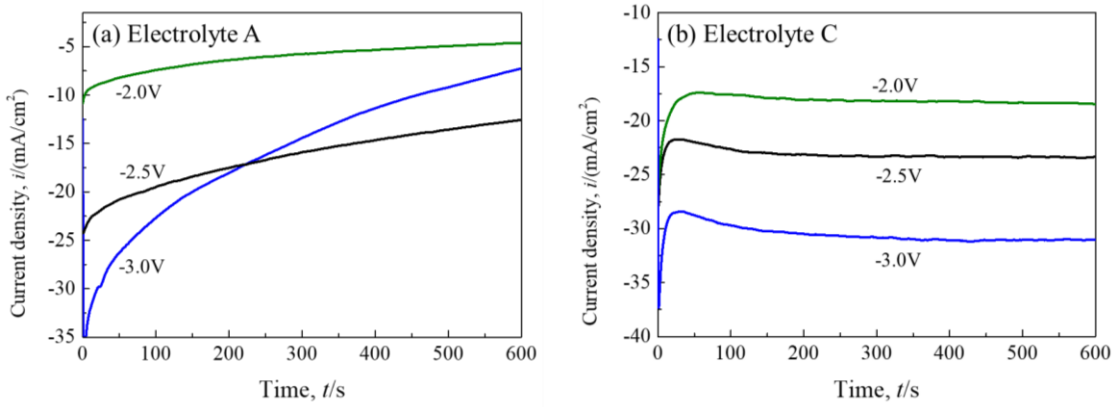

Fig. 2 Potentiostatic chronocurrent curves on a Cu plate at applied potentials of -2.0V, -2.5V and -3.0V (vs. SSE) in electrolytes A (a) and C (b).

3.3.2 Surface and Cross-section

Films A, B, and C were obtained from solutions A, B, and C, respectively. When deposition-finished film A was removed from the solution and immediately put into water to rinse, gas bubbled from the surface, accompanying the dissolution of the film. The effect was more intense in specimens deposited at higher negative-potentials.

Therefore, acetone was selected instead of water to rinse film A. With 1-day storage in a desiccator containing dry air, the film surface color changed from black to white. The higher the negative-potential applied, the wider the white-area that appeared. In contrast, films B and C were stable in either water or air.

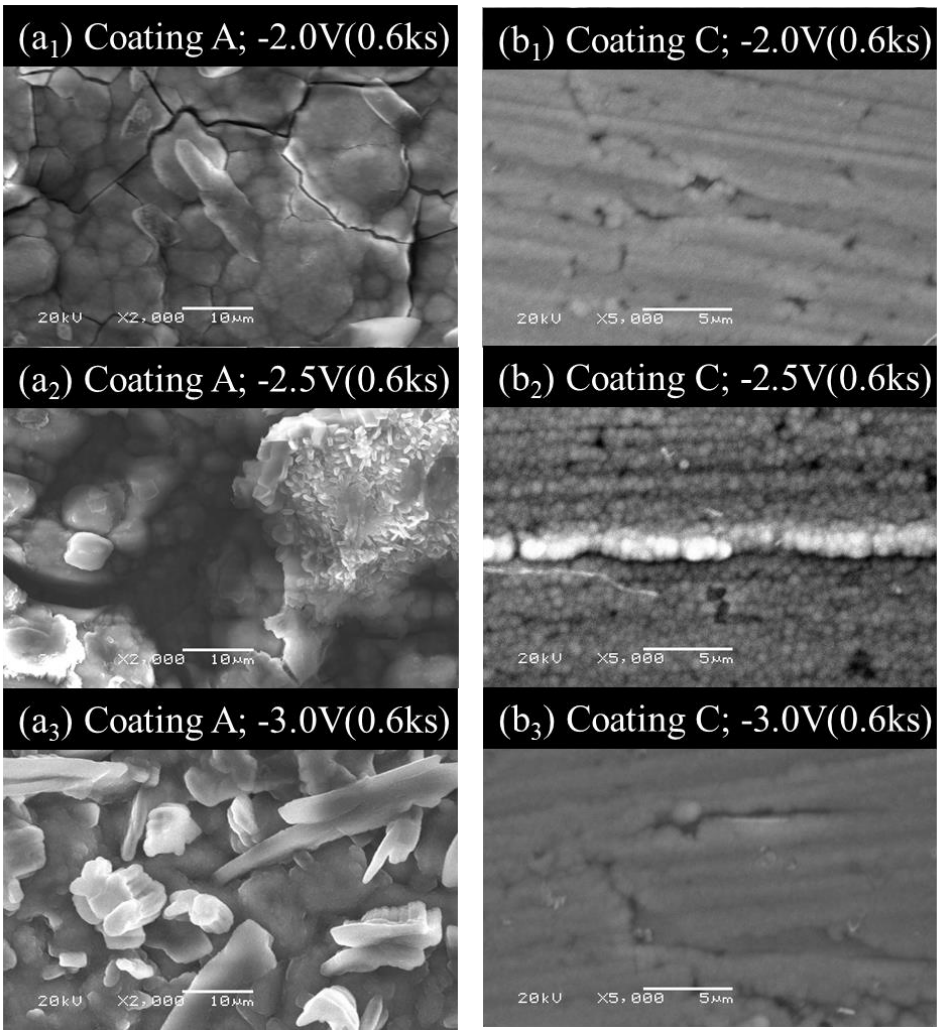

Fig. 3 Surface morphologies of films A (a) and C (b) deposited at -2.0 V, -2.5 V and -3.0 V (vs. SSE) for 0.6 ks.

Fig. 3 shows surface features of films A and C deposited at -2.0 V, -2.5 V, and -3.0 V (vs. SSE) for 0.6 ks. In film A (Fig. 3 a), rod- and lump-like particles were evident, along with some cracks. The fracture surface of the crack was examined in composition analysis in section 3.3.4. On film C (Fig. 3 b), uniform spherical particles were observed, and no cracks were present. The surface morphology of film B was

like that of film C (figure omitted).

Fig. 4 shows the cross-section of film C deposited at -2.0 V and -3.0 V. The thickness ranges from 0.5 to 2.0 μm depending on the potential applied and deposition duration. Higher negative-potential promoted film thickness. No delamination or vertical cracks are evident, resulting in good compactness and integrity. A comparative cross-section view of film A was unavailable due to equipment constraints (wire cut electrical discharge machine). In contrast, in film A (-2.5 V; 0.6 ks), a FIB-machined cross-sectional slice by TEM revealed two layers, an outer one (bright, thickness: 0.8 μm) and an inner one (grey, thickness: 2.7 μm) without delamination (Fig. 6 a1).

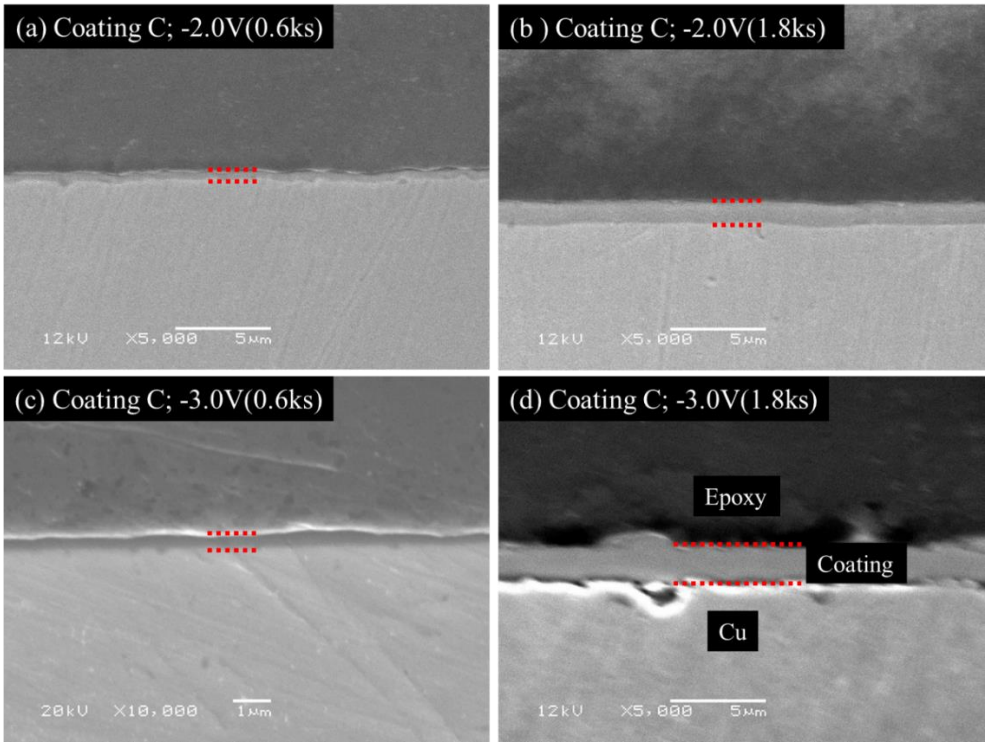

Fig. 4 Cross-section of films C deposited at -2.0V, and -3.0V (vs. SSE) for 0.6ks and 1.8ks.

3.3.3 Crystal Structure

Fig. 5 compares pre- and post-coated grazing incidence X-ray diffraction patterns. The diffraction peaks of Cu (111), (200), and (220) were detected in the copper plate.

Among film A, diffraction peaks of Li_2CO_3 (002), (402), and (424), or the peak of Li_2O (220) were confirmed. Higher negative-potential, higher diffraction peaks appeared. Under the same applied potential, -2.5 V or -3.0 V, for a longer deposition period, the diffraction intensity of Li_2CO_3 (002) and (402) became weaker. Conversely, these diffraction peaks at -2.0 V became more apparent with a longer deposition time. Diffraction patterns among film C significantly differed from those among film A. The longer the deposition time, the weaker the diffraction intensity, with peaks of Cu (200) and (220) almost absent from the 1.8 ks deposited specimen. No other peaks were detected. Therefore, film C was confirmed as both amorphous and crystalline. These XRD results correspond with previous reports, [1-6] where apparent crystallization can be obtained by post-heat treatment.

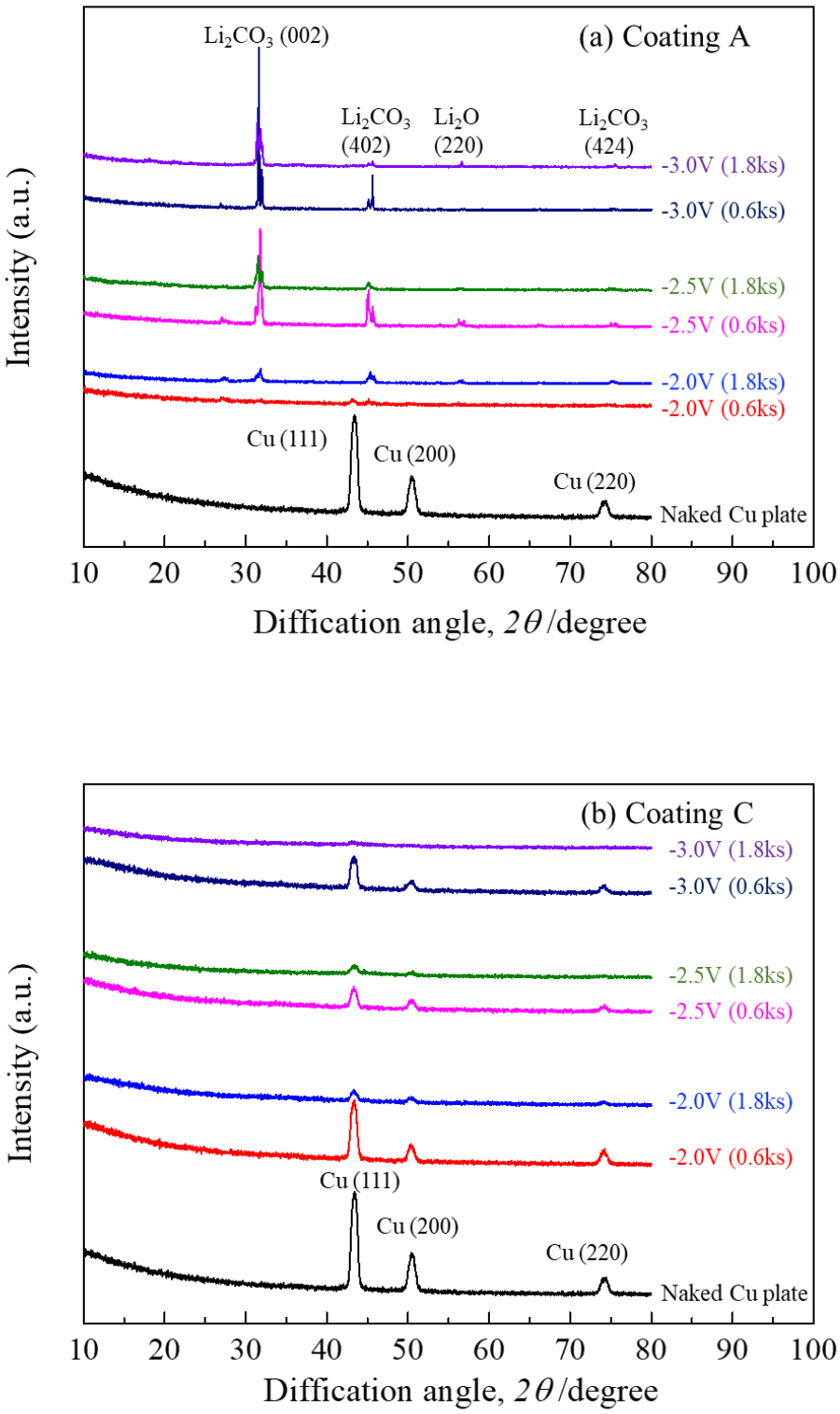

Fig. 5 Glancing X-ray diffraction patterns of films A (a) and C (b) deposited at -2.0V, -2.5V, and -3.0V (vs. SSE) for 0.6ks and 1.8ks, with an incidence angle of 1.0° .

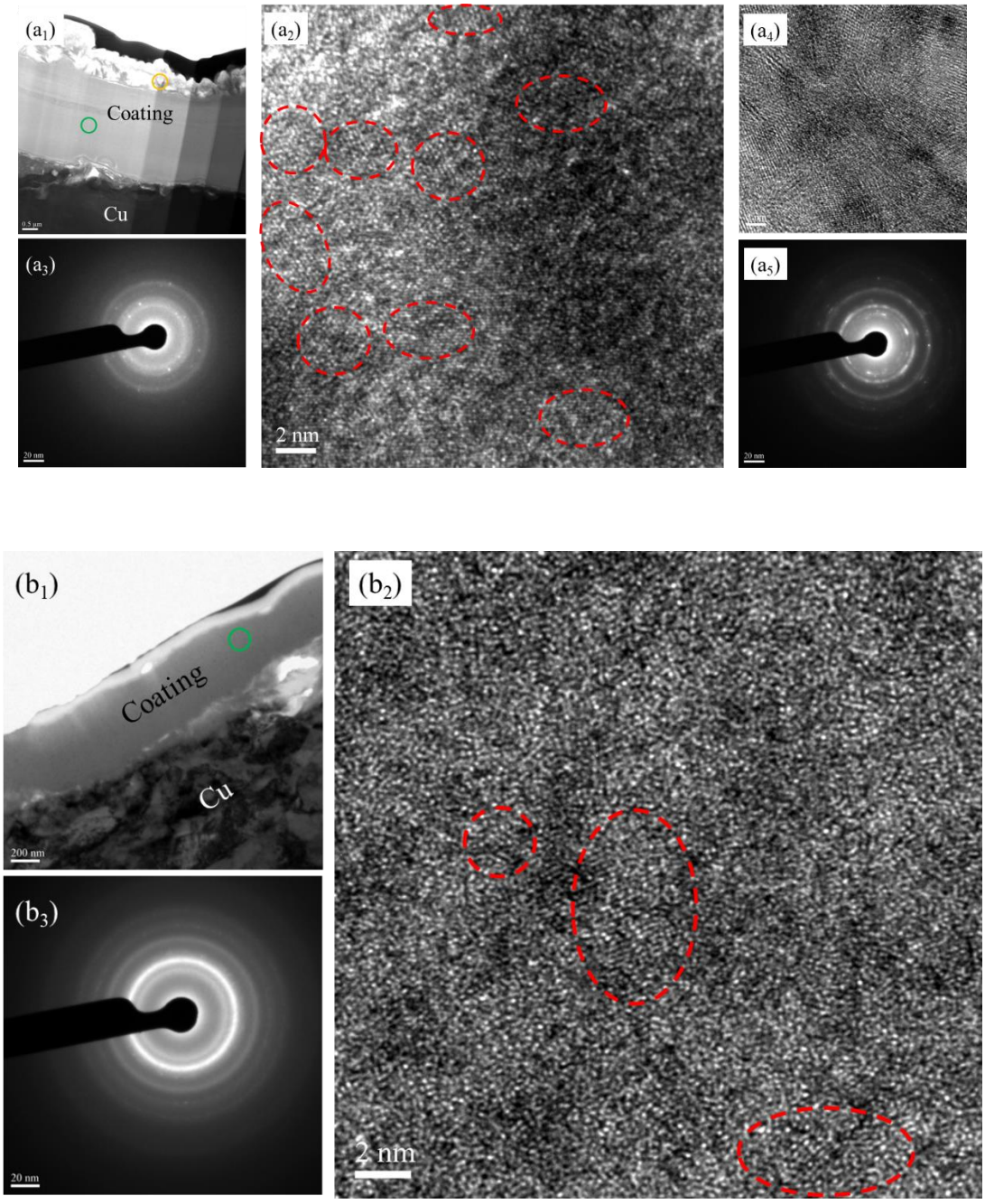

Fig. 6 Bright-field images at low magnification (a1, b1) and high magnification (a2, a4, b2) and selected area electron diffraction (SAED) patterns (a3, a5, b3) from the green circles (a1, b1) and orange circle (a1).

a1~a5: Film A obtained at -2.5 V (vs. SSE) for 0.6 ks; b1~b3: Film C obtained at -2.5 (vs. SSE) for 0.6 ks.

Fig. 6 shows the results of TEM analysis of cross-sectional slices of films A (-2.5 V, 0.6 ks) and C (-2.5 V, 0.6 ks). The bright-field images (a1, b1) confirmed that film A was thicker than film C. As described before, two layers were observed in film A. From the bright-field image (a2, b2), more nanocrystals were observed in the inner layer of film A than in C. The selected area electron diffraction (SAED) pattern (a3, b3) also confirmed a fine structure containing the main amorphous and some nanocrystals for either film C or the inner layer of film A. According to Fig. 6 a4 and a5, we know that the outer layer is almost completely composed of nanocrystals. These results agree with the XRD data in Fig. 5.

3.3.4 Composition and Chemical State

The composition of films was analyzed by SEM-EDS. Fig. 7 shows the molar fractions of Cr, Mn, Fe, Co, Ni, O, and C in films A, B, and C, which were obtained at -2.0 V, -2.5 V, and -3.0 V (vs. SSE) for 0.6 ks. The five targeted metal elements (Cr, Mn, Fe, Co, and Ni) in film A were approximately equal regardless of applied potential.

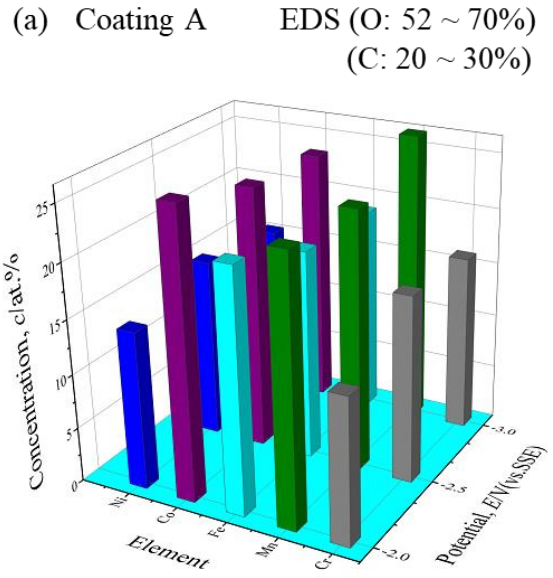

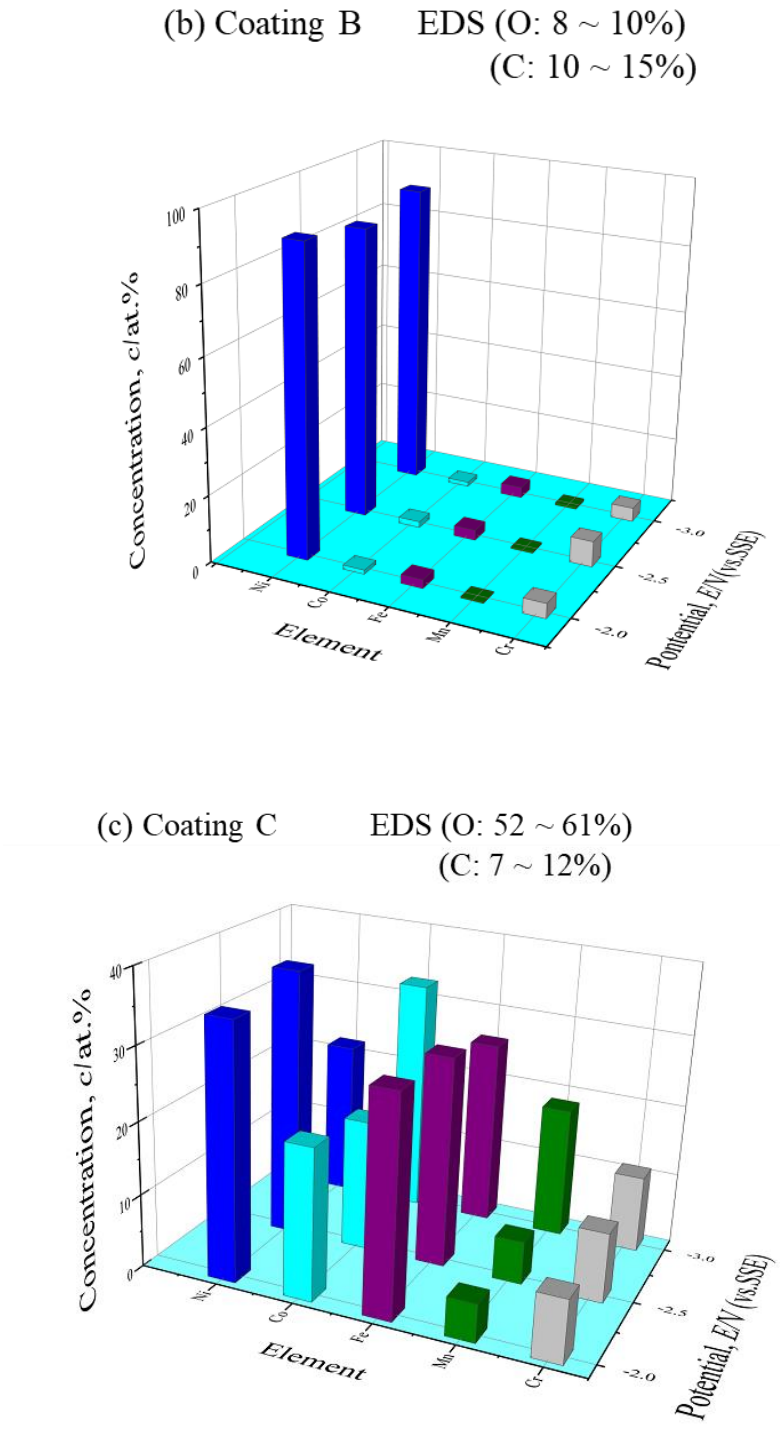

Fig. 7 Atomic percentage of elements in films A (a), B (b), and C (c) deposited at -2.0 V, -2.5 V and -3.0 V (vs. SSE) for 0.6 ks. The compositions were obtained by EDS.

Ni occupied the main component up to 90 at. % (atomic percentage) of the target metals in film B regardless of applied potential, resulting in much less co-deposition of the other four elements.

Table 2 Compositions and mixed configuration entropies (ΔSm_7, ΔSm_5) of films obtained in electrolyte C for 0.6 ks. ΔSm_7: containing elements O, C, Cr, Mn, Fe, Co, and Ni; ΔSm_5: containing elements Cr, Mn, Fe, Co, and Ni.

Applied potential	Atomic percentage of element (at. %)							ΔSm_7	ΔSm_5
(V vs. SSE)	Cr	Mn	Fe	Co	Ni	O	C	($J \cdot K^{-1} \cdot mol^{-1}$)	($J \cdot K^{-1} \cdot mol^{-1}$)
-2.0	4.74	4.58	7.14	5.41	12.8	52.57	12.76	1.50R	1.52R
-2.5	5.04	6.43	7.54	6.00	6.47	60.96	7.56	1.37R	1.60R
-3.0	5.66	2.09	8.16	5.32	10.23	55.61	12.93	1.43R	1.50R

R=8.314 J/(mol • K)

As applied potential decreased in film C, Ni and Fe decreased while Co and Mn increased. At an applied potential of -3.0 V, almost a similar content of the five metals was obtained in film C. Table 2 shows the compositions and mixed configuration entropies of film C after electrodeposition for 0.6 ks. Here, ΔSm_7 and ΔSm_5 are the mixing entropies calculated from all elements (C, O, Cr, Mn, Fe, Co, Ni) and from only five metals (Cr, Mn, Fe, Co, Ni), respectively. In both films A and C, there is more than 50 at. % oxygen was detected.

Figs. 8 and 9 show XPS spectra of films A and C after Ar+ sputter etching for 6.0 ks. The etched depth of about 20 nm (vs. SiO_2) was sufficient to remove contaminants.

Peak deconvolution was conducted for each chemical state. Only the central positions are shown for visual effect. From TEM observation (Fig. 6 a1), we know all the spectra for film A were obtained from the outer layer. In film A (-3.0 V, black lines), 2p peaks of Cr, Mn, Fe, Co, and Ni did not appear. In contrast, high O 1s and Li 1s were clearly detected. Further, from a preliminary TEM-EDS mapping of the cross-section, fewer elements, Cr, Mn, Fe, Co, and Ni, were detected in the outer rather than inner layer. Therefore, lithium may have been included in the film during electrodeposition and then formed the lithium-enriched outer layer afterward. This may explain the dissolution in water with bubbles. As described in section 3.1, Li^+ can be reduced to Li^0 in an isolated $LiClO_4$-containing solution at -3.0 V. Therefore, from analysis of C 1s, O 1s, and Li 1s, the formation of Li_2CO_3 and Li_2O can be confirmed in the outer layer. Li_2CO_3 and Li_2O correspond to binding energies 54.6 eV and 53.5 eV, respectively. Lithium generally combines O_2 and CO_2 in the air to form Li_2CO_3,

[10] which corresponds to the white appearance of the outer layer after air exposure. Large amounts of lithium in this film and subsequent formation of Li_2CO_3 and Li_2O may have led to local stress resulting in the cracks observed (Fig. 3 a3, b3). With the increased applied potential to -2.5 V or -2.0 V, the intensity of Li 1s may decrease, and the 2p spectra of Cr, Mn, Fe, Co, and Ni appear. The inclusion of lithium in films at -2.5 V was different from that obtained in the isolated $LiClO_4$-containing solution. Perhaps the reduction of Li^+ was promoted by other metal ions. At -2.0 V, the five 2p spectra of the target elements reached their highest values. Cr^{3+} and Mn^{2+} were observed at 576.6 eV and 641.3eV, but without the appearance of Cr^0 and Mn^0. Meanwhile, Fe 2p was deconvoluted into Fe^{3+}, Fe^{2+}, and Fe^0; Co^{2+}, Co^0, Ni^{2+}, and Ni^0 were respectively distinguished from Co 2p and Ni 2p. In addition, the O 1s spectrum can be deconvoluted into O(-Li), O(-M), and HO(-M). The corresponding binding energies [28] are listed in Table 3.

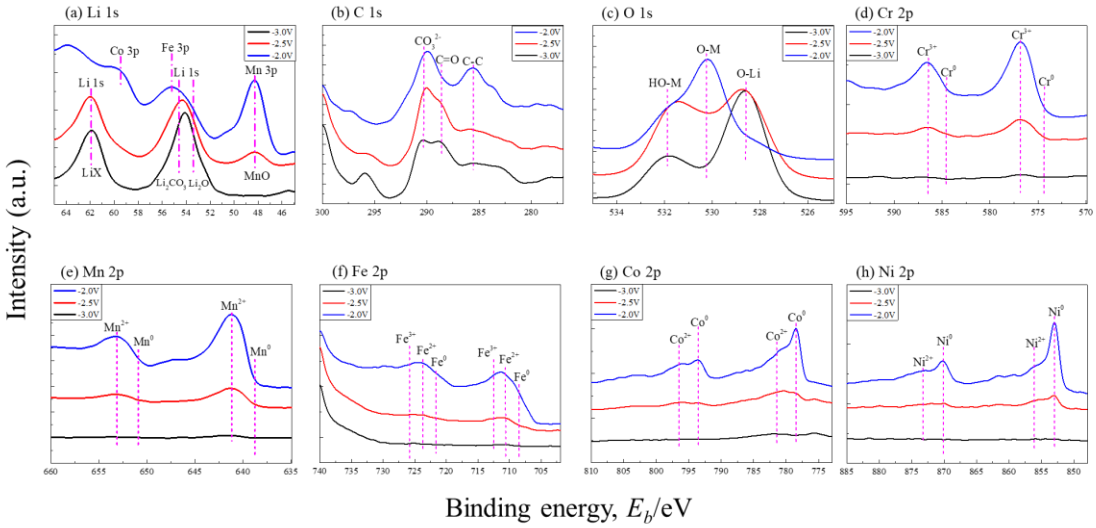

Fig. 8 XPS spectra of Li 1s, C 1 s, O 1s, Cr 2p, Mn 2p, Fe 2p, Co 2p, and Ni 2p from the films A obtained at -2.0V, -2.5V and -3.0V (vs. SSE) for 0.6ks. The analysis was conducted after Ar^+ sputter etching for 6.0ks.

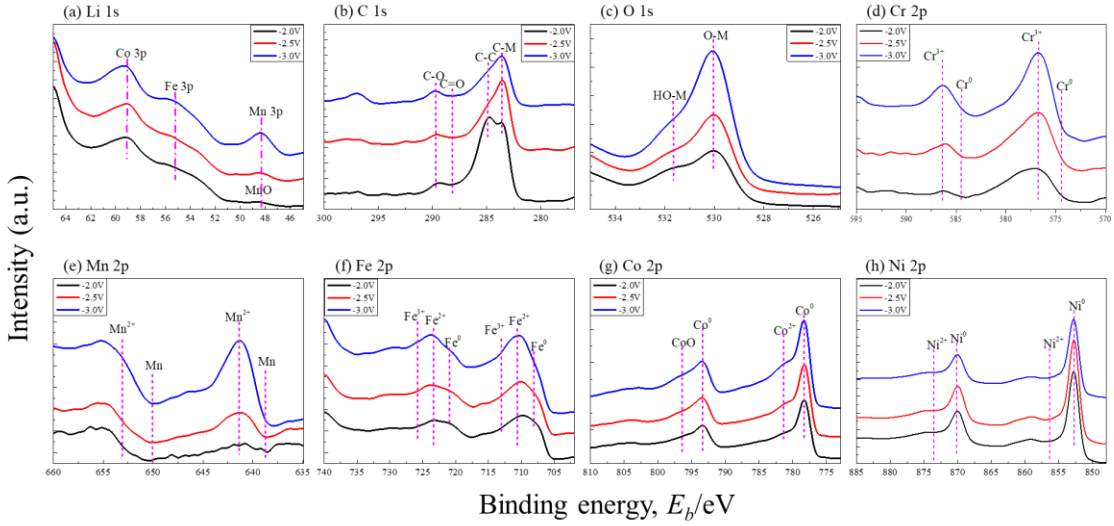

Fig. 9 XPS spectra of Li 1s, C 1s, O 1s, Cr 2p, Mn 2p, Fe 2p, Co 2p, and Ni 2p from the films C obtained at -2.0V, -2.5V and -3.0V (vs. SSE) for 0.6ks. The analysis was conducted after Ar^+ sputter etching for 6.0ks.

Table 3 Binding energies of Li 1 s, C 1s, O 1s, Cr 2p, Mn 2p, Fe 2p, Co 2p and Ni 2p spectrum and atomic sensitive factors used for quantitative determination. *ASF: Atomic sensitive factor

Photo peak	Li 1s		Cr 2p3/2	Mn 2p3/2	Fe 2p3/2			Co 2p3/2		Ni 2p3/2	
Component	Li_2O	Li_2CO_3	Cr^{3+}	Mn^{2+}	Fe^0	Fe^{2+}	Fe^{3+}	Co^0	Co^{2+}	Ni^0	Ni^{2+}
Binding energy (eV)	53.5	54.6	576.6	641.3	708.4	710.7	713.7	778.4	781.2	852.9	856.3

Photo peak	C 1s					O 1s		
Component	C-C	C=O	CO_3^{2-}	C-M	C-O	O-Li	O (-M)	O (-OH)
Binding energy (eV)	285.7	287.8	290.0	283.4	289.8	528.6	530.2	531.8

On either of films C (Fig. 9), the 2p spectra of Cr, Fe, Co, and Ni appeared. Mn peak was not detected at -2.0 V but was at -2.5 V and -3.0 V. Either of the above elements showed similar chemical states as film A (-2.0V vs. SSE). In Fig. 7 (a), except for the 3p spectra of Fe, Co, and Mn, the Li 1s peak did not appear due to the absence of $LiClO_4$ in the solution.

Fig. 10 shows atomic concentrations of elements at their detailed chemical states according to deconvoluted peaks. The symbol "M" means the five target metals without lithium. In film A (Fig. 10 a), C-C (organic contaminant), CO_3^{2-}, and C=O

were detected. For oxygen, compared to O(-M) and HO(-M), O(-Li) is the primary state. By decreasing the potential to -3.0 V, the Li content increased to near 55 at. %, while the total content of Cr, Mn, Fe, Co, and Ni sharply decreased to near zero. In film C (Fig. 10 b), except for Ni at -3.0 V, the contents of Cr, Mn, Fe, and Co gradually increased as the applied potential decreased. Only a little Ni^{2+} was detected as compared to Ni^{0}. Fe^{2+} and Fe^{3+} which occupied about 87% of total iron (9 - 11 at. %), while Co^{2+} was about a half of the total cobalt (11 at. %). For Cr and Mn, except Cr^{3+} and Mn^{2+}, no elemental Cr0 and Mn0 were detected. With the decrease of the potential, oxygen increased while carbon decreased. The total oxygen content was at 22 - 39 at.%, in which O(-M) was the main component. The XPS-analyzed oxygen concentration is about half of that EDS-analyzed one. Note that oxygen in the outer layer of film A existed mainly as Li_2CO_3 and Li_2O, while in film B, it mainly formed oxides and hydroxides of the target metals.

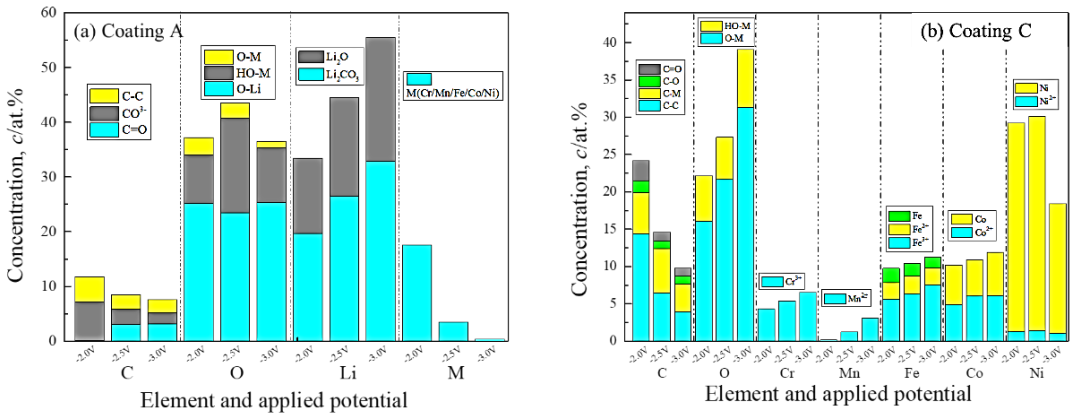

Fig. 10 Quantitative concentration of elements obtained from Figures 8 and 9 (XPS analysis).

Fig.11 shows mapping for lithium on a fracture surface of film A (-2.5 V vs. SSE; 0.6 ks). Lithium was detected from the film surface right through to the copper substrate, demonstrating that lithium was trapped within the whole of the film.

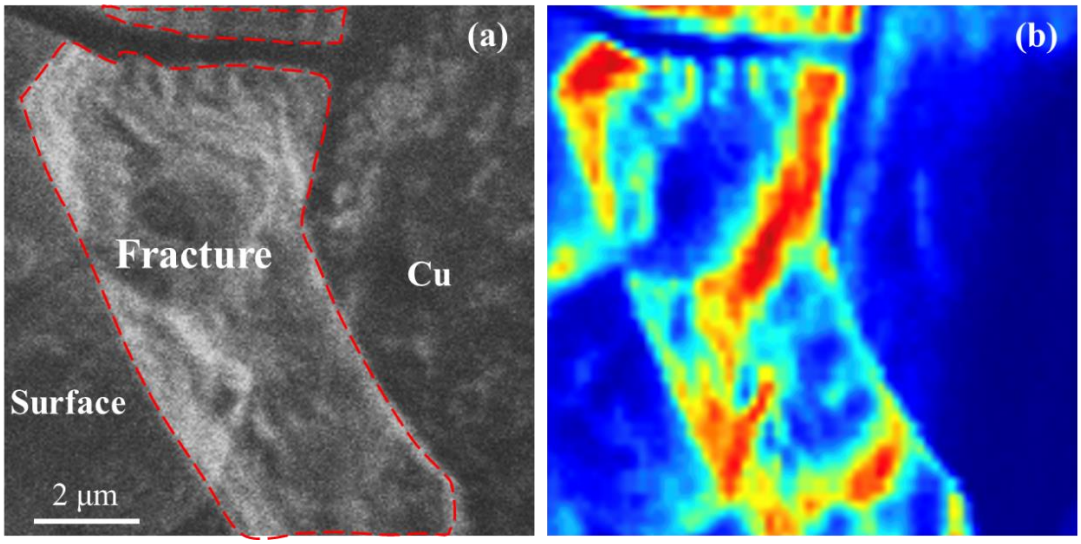

Fig. 11 A fracture surface of the film A (-2.5V vs. SSE; 0.6ks) and its lithium mapping by TOF-SIMS.

3.3.5 Reactions in Electrodeposition

In electrolyte A, Li^+ participates in constructing the electric double layer under a designated potential. With the initial deposition of M (Cr, Mn, Fe, Co, or Ni), more and more Li^+ concentrates in the electric double layer, leading to a reduction in target element deposition. When the lithium ions reach a threshold concentration, the reduction of Li^+ to Li^0 occurs. The inclusion of lithium in the film might also be related to the effect of co-deposition with other metal ions.

In electrolytes B or C, without Li^+ to participate in the electric double layer, the deposition current quickly became stable. The origin of contained oxygen in the film is a big issue. In a preliminary experiment using only anhydrous chemicals $MnCl_2$, $FeCl_2$, and $CoCl_2$, a MnFeCo film with near 50 at. % contained oxygen was confirmed. Therefore, it is reasonable to consider that the contained oxygen atoms came mainly from DMF (C_3H_7NO). However, the details are unclear and worth further investigation. On the other hand, the bound water in $CrCl_3 \cdot 6H_2O$, $FeCl_2 \cdot 4H_2O$, and $NiCl_2 \cdot 6H_2O$ should also provide some oxygen to the film according to the CV curves (Fig. 1 a). It is known that $CrCl_3 \cdot 6H_2O$ firstly ionized to a compact

octahedron structured $[Cr(H_2O)_6]^{3+}$ in the current solution.[12] Similar hydration or solvation phenomena might also occur for Mn^{2+}, Fe^{2+}, Co^{2+}, and Ni^{2+}. Such complexes should have varied the reduction potential of each of the metal ions and, therefore, affected the co-deposition behavior.

The complete formation of oxide/hydroxide of chromium and magnum indicates a possibility that reduction of Cr^{3+} and Mn^{2+} did not occur. Reduction peaks for Cr^{3+} were not detected, and the current peak at -2.70 V and -2.35 V vs. SSE in Fig.1 b and c might not correspond to the reduction of Mn^{2+}.

According to the above analysis, the synthesized films are not pure metals of CrMnFeCoNi but oxygen-containing ones, which contain some carbon atoms near that so-called HEO. The ratio of the high-valent metal of M^{m+}/M in film C decreased from Cr^{3+}/Cr, Mn^{2+}/Mn, Fe^{n+}/Fe, Co^{2+}/Co, to Ni^{2+}/Ni, seemingly related to a decrease in unpaired electrons in the 3d and 4s orbitals in the order of Cr, Mn, Fe, Co, and Ni. Oxygen atoms bound to all atoms of Cr and Mn, most atoms of Fe, half of Co, and a few Ni atoms, perhaps leaving a certain amount of oxygen vacancies. Analyses of X-ray diffraction and TEM suggest this film was almost amorphous without oxides with a uniform distribution of its elements. Furthermore, the supporting electrolyte of $LiClO_4$ was proven detrimental to the above electrodeposition. Knowledge obtained from this study can be applied to the deposition of other elements to pursue novel functions or properties.

3.3.6 Mechanical and electrocatalytic properties

Plastic hardness values of film C (deposition time: 1.8 ks) obtained under maximum load 40 nN were 2670 MPa (-2.0 V vs. SSE), 2660 MPa (-2.5 V), and 2250 MPa (-3.0 V), which exceed the copper substrate hardness of 1600 MPa.

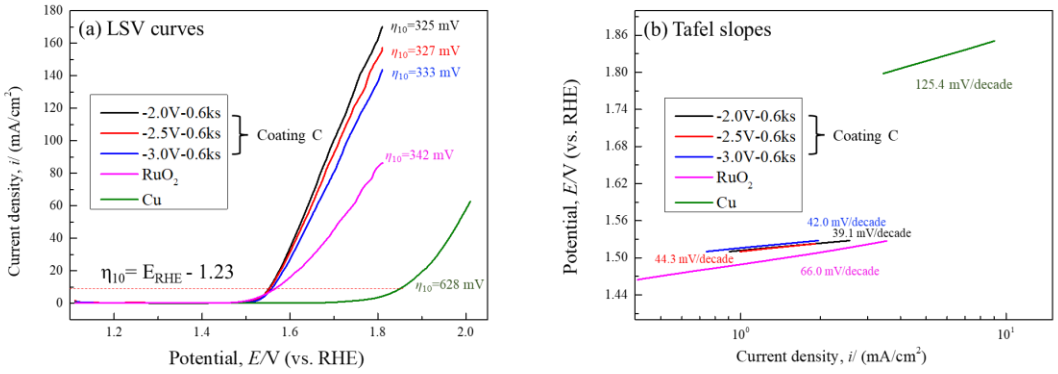

Fig. 12 Polarization LSV curves (a) and Tafel slopes (b) of Cu, RuO_2, and films C deposited at -2.0 V, -2.5 V, and -3.0 V (vs. SSE) for 0.6 ks.

Fig. 12 shows the polarization LSV curves (a) and the Tafel slopes (b) of Cu, RuO2, and films deposited at -2.0 V, -2.5 V, and -3.0 V (vs. SSE) for 0.6 ks in electrolyte C in 1.0 M KOH solution. The overpotential (η10) to the standard potential of $2H_2O = O_2 + 4H^+ + 4e^-$ (1.23 V vs. RHE), corresponding to the benchmark current density of 10 mA/cm2, was used to evaluate OER activity. Compared to 628 mV on Cu, the overpotential of 325-333 mV in film C shows high catalytic activity. Such overpotentials are apparently smaller than that of RuO_2 (342 mV). Furthermore, the Tafel slope (39.1 - 44.3 mV/decade) is also extremely lower than those of copper (125.4 mV/decade) and RuO_2 (109.6 mV/decade). These results indicate the potential for the use of oxygen-containing CrMnFeCoNi film instead of expensive RuO_2. Plenty of oxygen vacancies might have been produced due to the different oxidation states of Cr, Mn, Fe, Co, and Ni in the film, which attributed to this low overpotential for OER. The mechanism and stability of these films will be further investigated.

3.4 Conclusion

Several oxygens-containing CrMnFeCoNi films were prepared by electrodeposition in an organic solvent of DMF-CH_3CN with chlorides of chromium, manganese, iron, cobalt, and nickel. Support electrolyte $LiClO_4$ was included or excluded from the

solution to investigate the effect of Li^+ reduction. The composition and structure of the films were investigated, and the deposition process was discussed. Finally, mechanical and electrocatalytic properties were investigated. The obtained results were as follows:

(1) In the presence of $LiClO_4$ in the solution, lithium was contained in the film and then oxidized to Li_2CO_3 and Li_2O in the air. Therefore, $LiClO_4$ was unsuitable as a supporting electrolyte in the current deposition.

(2) In the absence of $LiClO_4$ in the solution, stable films were obtained by enhancing concentrations of target metal ions and applying constant potentials at -2.0, -2.5, and -3.0 V (vs. SSE). Resultant films were confirmed to be amorphous and nanocrystalline, containing more than half of oxygen atoms and near-equal ratios of Cr, Mn, Fe, Co, and Ni.

(3) Full oxide/hydroxide of Cr and Mn, most oxide/hydroxide of Fe, half oxide/hydroxide of Co, and some oxide/hydroxide of Ni composed the film, giving entropies of metal elements near or larger than 1.5 R.

(4) The oxygen-containing film CrMnFeCoNi showed a high hardness level and advanced electrocatalytic activity in the oxygen evolution reaction.

References

1) C. Yao, P. Zhang, M. Liu, G. Li, J. Ye, P. Liu, Y. Tong; Electrochim. Acta; 53, 8359-8365, 2008.

2) C. Yao, P. Zhang, Y. Tong, D. Xia, H. Ma; Chem. Res. Chinese Universities; 26, 640-644, 2010.

3) C. Yao, H. Ma, Y. Tong; Chinese Journal of Applied Chemistry; 28, 1189-1194, 2011.

4) H. Li, H. Sun, C. Wang, B. Wei, C. Yao, Y. Tong, H. Ma; J. Alloys Compd.; 598, 161-165, 2014.

5) M. Zheng, Y. Li, J. Hu, Y. Zhao, L. Yu; Mater. Sci.; 11, 344-348, 2014.

6) V. Soare, M. Buradaa, I. Constantin, D. Mitrică, V. Bădiliță, A. Caragea, M. Târcolea; Appl. Surf. Sci.; 358, 533-539, 2015.

7) J.E. House Jr, L. A. Reif Jr, J.D. House; Thermochim. Acta; 66, 365-368, 1983.

8) M. Tezuka; Chemistry and Education; 46, 222-225, 1998.

9) E. Gürbüz, V. Albin, V. Lair, A. Ringuedé, M. Cassir: Electrochim. Acta; 395, 139202, 2021.

10) Q. Tang, X. Dai, Z. Wang, F. Wu, Y. Mai, Y, Gu, Y. Deng; Ceram. Int.; 47, 19374-19383, 2021.

11) R. Wang, Y. Li, T. Xiao, L. Cong, Y. Ling, Z. Lu, C. Fukushima, I. Tsuchitori, M. Bazzaoui; Sci. Rep-UK; 9, 13094, 2019.

12) V. Protsenko, F. Danilov; Electrochim. Acta; 54, 5666-5672, 2009.

Chapter 4 Summary

The oil crisis and climate warming are the two significant issues affecting the world. Clean hydrogen energy must be developed to alleviate this series of problems. Among them, electrolysis of water is widely used as an effective mean to obtain hydrogen energy. However, the anodic catalyst material that limits the hydrogen generation rate is still the focus of breakthroughs. Among them, high-entropy alloy materials are widely studied as new materials in the research of anode materials. For constructing the hydrogen society both in practical application and academic investigation, it is essential to explore novel catalyst materials with complex components and structures to achieve high catalytic activity and stable/long life for oxygen evolution reaction (OER) and to develop simple and low-cost synthesis method of the catalytic electrode for large scale applications in water electrolysis. As a resource-saving and straightforward method, the electroplating method is expected to be an effective method to reduce the complexity of the preparation process of high-entropy materials and directly use them as electrode materials. Here, in this study, oxygen-containing CrMnFeCoNi high-entropy alloy films were synthesized in organic solutions of DMF and CH_3CN using Cr, Mn, Fe, Co, and Ni chlorides. The film formation mechanism and the OER performance of this oxygen-containing CrMnFeCoNi high entropy film were discussed.

This paper consists of 4 chapters, including an introduction and a summary. The outline of each chapter is shown as follows.

Chapter 1 explained the characteristics of hydrogen, summarized the research background and the current trend on high-entropy materials, and described the purpose and characteristics of this thesis.

In Chapter 2, two films containing Cr, Mn, Fe, Co, Ni, O, and C were electrodeposited on a copper plate in an organic solvent of DMF (N, N-dimethylformamide) and CH_3CN (acetonitrile) without and with the supporting electrolyte of $LiClO_4$. The surface morphologies, components, and crystal structures

of the oxygen-containing film were analyzed by SEM, XRD, EDS, TOF-SIMS, and TEM. An amorphous structure mixed with nanocrystals was detected in film A. On the other hand, film B obtained in solution with $LiClO_4$ can be divided into an inner layer, an intermediate layer, and an outer layer. Lithium oxide in the inner layer and lithium oxide/carbonate in the outer layer were detected. The uniform spatial distribution of Cr, Mn, Fe, Co, and Ni was mainly contained in the intermediate layer. Film B is easily delaminated from copper in water and unstable to electron irradiation.

In Chapter 3, oxygen-containing CrMnFeCoNi films were electrodeposited in an organic solvent of DMF-CH_3CN, with or without $LiClO_4$, to investigate the detailed effect of lithium ions. The composition, structure, hardness, and electrocatalytic properties of the films were examined. The presence of lithium in films obtained with $LiClO_4$ showed it to be unsuitable as a supporting electrolyte in this fabrication process. Without $LiClO_4$, oxygen-containing CrMnFeCoNi films were obtained by enhancing the concentrations of the target metal ions in the solution. These films were mainly amorphous with some nanocrystals, which were comprised of > 50 atom % oxygen atoms and near equiatomic Cr, Mn, Fe, Co, and Ni, showing a high level of hardness and advanced electrocatalytic activity in the oxygen evolution reaction (OER).

Chapter 4 summarizes the conclusions obtained from this study.

In a summary, this study successfully synthesized oxygen-containing CrMnFeCoNi films with high catalytic performance as an oxygen evolution electrode in water hydrolysis.

Acknowledgment

I would like to express my deepest gratitude to Professor Rongguang Wang, Graduate School of Science and Technology, Hiroshima Institute of Technology, for his kind supervision and the encouragement throughout this research.

I would like to thank the Professor Takeshi Tanaka, Professor Makoto Hino, and Professor Yoshikazu Hiraga of Hiroshima Institute of Technology, who were the sub-chief examiners for my doctoral dissertation.

I would like to thank the professors of the Graduate School of Science and Technology, Hiroshima Institute of Technology, who have taught me various things during my classes. I would like to express my sincere gratitude to Wen Zhou of Guangxi University for his assistance in the study of XRD measurements. I would like to express my sincere appreciation to Eishi Tanabe of the Hiroshima Prefectural Research Institute of Technology for his assistance in the research on TEM and TOF-SIMS measurements. As an international student, I would like to express my gratitude to the staff at the Center for International Exchange for their continued cooperation in checking my scholarship application documents.

Last but not least, thank my parents for supporting my studies in Japan.

Publication list

[学位に係る論文]

1

Tian Xiao, Rongguang Wang, Eishi Tanabe, Yuhki Satoh, Mohammed Bazzaoui, Yunhan Ling, Zhaoxia Lu, Fabrication and Characterization of Oxygen-Carbon-Contained CrMnFeCoNi Coatings Electrodeposited in DMF-CH_3CN Solution with and without Supporting Electrolyte $LiClO_4$, Coatings, 12・12・1804(1-16), 2022.

2

肖 天, 王 栄光, 田辺 栄司, 有機溶媒を用いた CrMnFeCoNi 含有皮膜の電析による合成: 支持電解質 $LiClO_4$ の影響, 表面技術, 74・4・225-233, 2023.

[関連論文]

1

Rongguang Wang, Yunhui Li, Tian Xiao, Li Cong, Yunhan Ling, Zhaoxia Lu, Chiharu Fukushima, IsaoTsuchitori, Mohammed Bazzaoui, Using Atomic Force Microscopy to Measure Thickness of Passive Film on Stainless Steel Immersed in Aqueous Solution, Scientific Reports, 9・13094, 2019.

2

Qingyun Zhou, Yunhan Ling, Zhaoxia Lu, Mengyuan Zhang, Zhengjun Zhang, Tian Xiao, Rongguang Wang, Effect of Helium Implantation on the Hydrogen Retention of Cr_2O_3 Films Formed in an Ultra-low Oxygen Environment International Journal of Hydrogen Energy, 44・48・26685-26697, 2019.

3

Rongguang Wang, Yasunori Satake, Yunhui Li, Tian Xiao, Masaharu Honda, Hideki Fukuhara, Seiya Hiramatsu, Microstructure of Ni-Based Hard Facing Alloy and its

Polarization Behavior in Aqueous Solution with Different pH and Chloride Concentration, Corrosion Communications, 3・1-9, 2021.

4

Rongguang Wang, Yuto Ohgata, Yunhui Li, Tian Xiao, Masaharu Honda, Tribocorrosion Behaviour of SUS430 Stainless Steel in Aqueous Solutions with Different pH, Coatings, 13・9・1539, 2023.

5

王 栄光, 肖 天, 大川 歩夢, ハイエントロピー酸炭化物皮膜の電析による作製と酸素発生用電極への適用, クリーンエネルギー, 32・3・34-41, 2023.

[国際学会]

1

Tian Xiao, Rongguang Wang, Electrodeposition of CrMnFeCoNi Film in Organic Electrolyte with and without $LiClO_4$, INTERFINISH2020, A-SEP07-008, September 2021.

[国内学会]

1

肖 天, 鎌田 壮平, 王 栄光, 電析法による CrMnFeCoNi ハイエントロピー合金皮膜の創製と成分分析, 日本鉄鋼協会・日本金属学会中国四国支部鉄鋼第 64 回・金属第 61 回合同講演大会, A15, 2021

2

鎌田 壮平, 肖 天, 王 栄光, 放電プラズマ焼結法を用いた CrMnFeCoNi 合金の作製と変形抵抗・耐食性の測定, 日本鉄鋼協会・日本金属学会中国四国支部鉄鋼第 64 回・金属第 61 回合同講演大会, C04, 2021

3

肖 天, 王 栄光, DMF-CH_3CN 溶液を用いた酸素含有型 CrMnFeCoNi 電析皮膜の合成とサポート電解質 $LiClO_4$ の影響, 表面技術協会第 145 回講演大会, 08A-26, 2022

4

肖 天, 王 栄光, DMF-CH_3CN 溶液を用いた酸素含有 CrMnFeCoNi 電析皮膜の合成と酸素発生触媒への適用, 日本金属学会 2022 年春期（第 170 回）講演大会, 182, 2022

5

鎌田 壮平, 肖 天, 王 栄光, 放電焼結した CrMnFeCoNi 合金の元素分布と腐食溶出挙動, 日本機械学会 中国四国支部第 60 期総会・講演会, 03a1, 2022

6

肖 天, 王 栄光, 有機溶媒を用いた酸素含有型 CrMnFeCoNi 電析皮膜の合成と酸素発生触媒活性評価, 日本設計工学会中国支部講演論文集, 38 12-13, 2022

7

大川 歩夢, 肖 天, 王 栄光, 有機溶媒 DMSO を用いたハイエントロピー酸炭化物皮膜の合成と酸素発生触媒活性化評価, 腐食防食協会中国・四国支部「材料と環境研究発表会」講演集, 5-8, 2023

8

肖 天, 王 栄光, CrMnFeCoNi 酸炭化電析皮膜の構造解析と酸素発生触媒活性評価, 表面技術協会第 148 回講演大会, 04D-24, 2023